Aeroacoustic analysis based on FW–H analogy to predict low-frequency in-plane harmonic noise of a helicopter rotor in hover

T. SURESH, O. SZULC, P. FLASZYNSKI

Institute of Fluid-Flow Machinery, Polish Academy of Sciences, Fiszera 14, 80-231 Gdansk, e-mail: thanushree.suresh@imp.gda.pl

THE INTEGRAL FORMULATION OF THE FFOWCS-WILLIAMS AND HAWKINGS (FW–H) analogy, developed by Farassat (known as Farassat's formulation 1A), is implemented to study the sound generation and propagation of rotating slender bodies. The general post-processing numerical code utilizes the linear acoustic theory to predict the thickness and loading noise terms for bodies in subsonic motion. The developed numerical code is validated for elementary acoustic sources (rotating monopole and dipole) against analytical solutions. The validated code is then applied for prediction of low-frequency in-plane harmonic noise (LF-IPH) of a model helicopter rotor of Sargent and Schmitz in a low-thrust hover with full-scale tip Mach number. The required loading distribution of the rotor blade is obtained with CFD (RANS) and Blade Element Momentum Theory (BEMT) methods and also validated against literature data. The developed acoustic code, supplemented by CFD and BEMT loading analyses, allows for a detailed comparison (thickness and loading, near- and far-field, etc.) of the LF-IPH noise of a helicopter rotor in both, time and frequency domains. The predicted (FW–H) acoustic signals are compared not only with the reference code solutions, but also with the experimental data. Moreover, the paper quantifies the impact of computational grid density and time-step size (used by CFD and FW–H codes) on the final solution accuracy. Additionally, a simplified analytical code is developed (based on elementary dipole solutions, compact chord assumption and BEMT method) allowing for the initial loading noise analysis with highly reduced computational resources. The acquired results are fully compatible with the classical FW–H analysis in terms of the impact of the in-plane and out-of-plane forces on the generated noise. The FW–H code predictions of the acoustic pressure and its components are in satisfactory agreement with the reference and experimental data of Sargent and Schmitz.

Key words: Lighthill's analogy, Farassat's formulation, Blade Element Momentum Theory, Computational Aeroacoustics, Computational Fluid Dynamics, thickness noise (monopole), loading noise (dipole).

Notation

α angle of attack,
η source position in space,
μ_0 ambient viscosity,

ρ	density,
ρ_0	ambient density,
σ_{ij}	viscous stress tensor,
τ	source/emission time,
$\delta(f)$	Dirac delta function,
δ_{ij}	Kronecker delta,
$\square$	d'Alembert/wave operator,
Δt	time-step,
$\cos\theta$	local angle between normal to the surface and radiation vector,
$\hat{r}_i$	unit radiation vector,
Ω	specific rate of dissipation,
ω	vorticity magnitude,
θ	collective pitch angle,
$\vec{F}$	force vector,
$\vec{M}$	Mach number vector,
$\vec{r}$	radiation vector,
$\vec{U}_{in}$	Freude inflow velocity vector,
$\vec{U}_{out}$	Freude ouflow velocity vector,
$\hat{e}_{in}$	unit vector pointing towards the rotation center,
$\hat{e}_{out}$	unit vector pointing outwards,
A_{rotor}	rotor disc area,
AR	aspect ratio,
c	chord,
c_0	speed of sound,
c_{d0}	drag coefficient at $0°$ angle of attack,
c_d	drag coefficient,
c_l	lift coefficient,
$c_{l\alpha}$	lift coeficcient at angle of attack α,
c_p	pressure distribution,
c_q	torque coefficient,
c_t	thrust coefficient,
d_{in}	distance from the rotation center,
dS	elemental area,
f	moving surface; frequency,
f_A	amplitude,
F_d	drag force,
F_l	lift force,
F_Q	rotor shaft torque,
f_{rot}	frequency of rotation,
F	force,
F_T	rotor thrust force,
GCI	Grid Convergence Index,
k	turbulence kinetic energy,
L	total time of frequency analysis,
M	Mach number,
M_i	Mach vector components,
M_r	Mach number in the the direction of the observer,
M_T	tip Mach number,
n_i	components of the normal vector,
N	number of samples,
OASPL	Overall Sound Pressure Level,

p	pressure,
p'	acoustic pressure,
P_0	ambient pressure,
P_{ij}	pressure stress tensor,
p_L	loading noise pressure,
p_{rms}	root mean square pressure,
p_T	thickness noise pressure,
P_{ref}	reference pressure,
Q	volumetric mass-flux,
q	mass flow rate,
R	blade radius, rotation arm,
r	radial position along the blade; magnitude of the radiation vector ($\vec{r}$),
Re	Reynolds number,
RPM	rotational speed,
S	surface area,
SPL	Sound Pressure Level,
T	time period,
t	observer/physical time,
T_0	ambient temperature,
T_{ij}	Lighthill's stress tensor,
u_i	velocity components,
v_n	normal velocity,
V	volume, local flow velocity,
V_T	tip velocity,
x	observer space,
y_e	emission position,
y_i	fixed-frame system.

1. Introduction

Sound emission of helicopters, often operating at low altitudes, causes community annoyance and hindrance to daily life for people living around airports. It is of even higher concern in military and medical applications which led to a push for "quiet helicopters". Increasingly over time, a global initiative to reduce noise levels that cause environmental and psychological concerns to human beings [1] has led to innovative noise mitigation strategies [2–4]. Noise control is a design parameter rather than a post production fix.

There are many physical mechanisms responsible for sound generation by a rotating body [5]. For example, in case of helicopter rotors operating in subsonic conditions (no transonic flow and shock waves), sound is generated due to blade thickness, blade loading, blade-vortex interaction (impulsive), blade self-noise, turbulence ingestion, and blade-wake interaction phenomena [6–9]. The harmonic (deterministic) noise, consisting of thickness and non-impulsive loading (steady) contributions, is present in all flight conditions (even in hover) and is called discrete frequency (tonal) rotational noise [5, 10]. There are two main chal-

lenges facing the noise mitigation goals. Firstly, the physics and mechanism of sound generation and propagation need to be sufficiently understood. Secondly, noise control without compromising the performance is difficult. There are also additional industrial constraints such as feasibility, extra weight, maintenance etc., which lead to "what is an acceptable compromise between performance and noise level reduction?" This has motivated extensive research programs in rotorcraft aeroacoustics (e.g. [2, 11, 12]).

Several approaches are available to predict numerically acoustic fields, with Computational Aero-Acoustics (CAA) being the most widely used option [13]. The advancements in computer capabilities have provided a strong impetus to CAA [14–16]. The acoustic fields can be analyzed by either a direct method, where the classical flow equations are solved [17] or through hybrid methods, where the sources (sound generation) are identified with CFD and the far-field sound propagation is treated through acoustic analogies [18]. However, there is a large disparity in the magnitudes between the acoustic and the flow characteristic scales making the direct methods cumbersome and computationally expensive. Hybrid methods offer elegant solutions by separating sound generation and sound propagation mechanisms [19]. This has led to development of several acoustic formulations over the years with a varying degree of success in predicting the sound emission and transmission for various applications [20–23]. Depending on the flow regime under study and the primary type of noise contributor (broadband or tonal), linear or non-linear effects are included in the acoustic formulation. Not only the acoustic models provide useful insights into the noise generation mechanisms [24], but also enable development of noise control strategies [25–27].

An in-house acoustic code is developed based on the Ffowcs Williams–Hawkings (FW–H) acoustic analogy [22] and Farassat's Formulation 1A (retarded time) [28]. It predicts acoustic pressure signals (and its components) in time domain based on the rotating body geometry, kinematics and surface loading (forces distribution) as inputs for arbitrary observer locations. This paper presents details of the development of the FW–H acoustic code based on the Farassat's Formulation 1A (surface integral). Firstly, the code is validated against analytical solutions for elementary acoustic sources [29]. The rotating source-sink pair case is designed as a simplified model of thickness (monopole) noise generation, while the rotating point force case mimics the mechanisms of loading (dipole) noise emission. Next, the validated code is utilized for the investigation of acoustic radiation of a model helicopter rotor operating in hover conditions. At this stage, two methods of blade loading distribution prediction are presented in detail: BEMT and CFD/RANS (FLOWer solver). The resultant acoustic pressure signals are compared with not only the reference code, but also the experimental data, both obtained at the University of Maryland [30].

2. Theoretical modeling

For rotating bodies, such as helicopter rotor blades in hover (subsonic motion), the low-frequency harmonic noise radiation consists of two main generation mechanisms [31]. The displacement of the fluid by the moving body causes thickness noise (monopole) and the surface forces (steady or unsteady) lead to loading noise (dipole) emissions [6, 23]. The monopole and dipole components are supplemented by the volumetric source (quadrupole), generated due to turbulence. It was introduced by Lighthill to study jet noise [20]. However, for helicopter rotors operating in subsonic conditions, the quadrupole generation is of tertiary importance only and may be neglected [10]. It is important to note that this simplification is not applicable at higher Mach numbers, when shock waves are developing at the blade tip (transonic flow) and quadrupole mechanism becomes dominating, e.g. in a high-speed forward flight.

2.1. Elementary point sources

The thickness noise source term (monopole) was proposed by Ffowcs Williams and Hawkings to account for the presence of solid bodies in arbitrary motion [22]. It is defined as a time derivative of elementary mass source, accounting for the displacement effect of the fluid produced by the body movement. To understand the thickness noise (monopole) generation, the solution to a simple 1D wave equation (Eq. (2.1)) for a pulsating and translating sphere (elementary source) is derived [29]. Acoustic pressure is defined as the local pressure deviation from the ambient atmospheric pressure caused by a sound wave

$$\Box^2 p' = \frac{1}{c_0^2}\frac{\partial^2 p}{\partial \tau^2} - \nabla^2 p' = \text{Sources}, \qquad (2.1)$$

where $\Box$, p', c_0, τ, ∇ are the D'Alembert/wave operator, acoustic pressure [Pa], speed of sound [m/s], source time [s] and nabla operator respectively.

Consider a point source of strength $Q(t)$ [m^3/s] in a compact volume region (V) enclosed by a surface (S) moving subsonically. Using Taylor series expansion of Green's function the sound source can be replaced by equivalent monopole [32]. The analytical solution for the sound radiated by a moving monopole as received by a stationary observer is given by Eq. (2.2) [29]

$$4\pi p'(x,t) = \left[\frac{\rho_0 \dot{Q}}{r(1-M_r)^2} + \rho_0 Q\frac{\vec{r}\cdot\vec{M} + c_0(M_r - M^2)}{r^2(1-M_r)^3}\right]_{ret}, \qquad (2.2)$$

where (x,t), ρ_0, $\dot{Q}$, $\vec{r}$, M_r, $\vec{M}$ and $\vec{M}$ are the observer time-space, density, source time derivative of volumetric mass-flux, radiation vector, the Mach number in

the direction of the observer, source time derivative of the Mach vector and the Mach vector respectively. When the variables r and M are denoted as scalars, it implies that the magnitude of their respective vectors are utilized.

The loading noise source term (dipole) was introduced by Curle to account for the unsteady loading forces exerted by the body on the fluid [21]. The study was devoted to the analysis of noise generation due to turbulent fluctuations present on a solid body. It is defined as a single doublet of equal forces of opposite phase [33]. A dipole is modeled as a moving point force (steady or unsteady). Utilizing the concepts of a far-field approximation, multipole expansion and boundary conditions, the analytical solution for sound radiated by a moving dipole (for a stationary listener) is given by Eq. (2.3) [29]

$$(2.3) \qquad 4\pi p'(x,t) = \left[\frac{\vec{r}\cdot\dot{\vec{F}} - c_0 \vec{M}\cdot\vec{F}}{c_0 r^2 (1-M_r)^2} + (\vec{r}\cdot\vec{F}) \frac{\vec{r}\cdot\dot{\vec{M}} + c_0(1-M^2)}{c_0 r^3 (1-M_r)^3} \right]_{ret},$$

where $\vec{F}$ and $\dot{\vec{F}}$ are the force vector and the source time derivative of the force vector, respectively. It is important to note that $\dot{\vec{F}}$ in the above equation are both space and time varying.

2.2. Ffowcs Williams–Hawkings (FW–H) acoustic analogy

The central idea of acoustic analogy is to decouple sound generation from sound propagation mechanisms [20]. Sound generation is modeled by the non-zero source terms of the inhomogeneous wave equation. Complex, non-linear noise radiating flow processes are reduced to equivalent elementary acoustic sources with linear propagation of sound in stationary medium of constant properties. Starting from the general wave equation (Eq. (2.1)), the acoustic analogy is obtained by rearranging the conservation equations of mass and momentum [32]. Ffowcs Williams and Hawkings introduced a novel idea of embedding the flow problem in an unbounded domain and applying generalized fuctions to solve the nonlinear aeroacoustic problem [22]. The moving body $(f(x,t) = 0)$ is enclosed in a control volume within which all the flow variables are defined (Fig. 1), thus allowing for Green's functions approach to be utilized (with proper boundary conditions) [21].

Ffowcs Williams and Hawkings provide an in-depth analysis of the underlying novel concepts in [22], while simplified derivations are discussed by Farassat in [28, 34]. The generalized form of FW–H equation presented in [22] is expressed by

$$(2.4) \qquad \Box^2 p' = \frac{\partial}{\partial\tau}[\rho_0 v_n \mid \nabla f \mid \delta(f)] - \frac{\partial}{\partial y_i}\left[P_{ij} \frac{\partial f}{\partial y_j} \delta(f) \right] + \frac{\partial^2 T_{ij}}{\partial y_i \partial y_j},$$

with $T_{ij} = \rho u_i u_j - \sigma_{ij} + (p - c_0^2\rho)\delta_{ij}$. v_n, $\delta(f)$, y_i, P_{ij}, T_{ij}, u_i, σ_{ij}, δ_{ij} are the normal velocity, the Dirac delta function, a fixed-frame system, a pressure tensor, the

Lighthill stress tensor, velocity components, a viscous stress tensor and the Kronecker delta, respectively. The sound generation is expressed as a linear sum of three source terms on the right hand side of Eq. (2.4), namely, monopole, dipole and quadrupole, respectively. Flow non-linearities are represented by Lighthill's stress tensor T_{ij} which can be neglected for a subsonic motion [33].

Out of several existing approaches to application of Eq. (2.4), the most widely used are integral solutions (analytical) proposed by Farassat, specifically derived for bodies in a subsonic motion. Utilizing the acoustic compactness condition for moving bodies and the far-field approximation, Farassat derived Eqs. (2.5) and (2.6), widely known as Formulation 1A [28]

$$(2.5) \qquad 4\pi p_T(x, t) = \int_{f=0} \left[\frac{\rho_0 \dot{v}_n}{r(1 - M_r)^2} + \frac{\rho_0 v_n \hat{r}_i \dot{M}_i}{r(1 - M_r)^3} \right]_\tau dS$$

$$+ \int_{f=0} \left[\frac{\rho_0 c_0 v_n (M_r - M^2)}{r^2 (1 - M_r)^3} \right]_\tau dS,$$

$$(2.6) \qquad 4\pi p_L(x, t) = \int_{f=0} \left[\frac{\dot{p} \cos \theta}{c_0 r (1 - M_r)^2} + \frac{\hat{r}_i \dot{M}_i p \cos \theta}{c_0 r (1 - M_r)^3} \right]_\tau dS$$

$$+ \int_{f=0} \left[\frac{p(\cos \theta - M_i n_i)}{r^2 (1 - M_r)^2} + \frac{(M_r - M^2) p \cos \theta}{r^2 (1 - M_r)^3} \right]_\tau dS,$$

where p_T, f, $\hat{r}_i$, M_i, dS, p_L and $\cos \theta$ represent the thickness noise term, moving surface, unit radiation vector, Mach vector components, elemental area, loading term, and the local angle between normal to the surface and radiation vector at emission time, respectively. The dot above a variable indicates the source time differentiation.

The total pressure signal is expressed as a sum of thickness noise p_T (Eq. (2.5)) and loading noise p_L (Eq. (2.6)) contributions. Each of these noise signals can be further decomposed as far-field (of the order $1/r$) and near-field (of the order $1/r^2$) terms. The effect of motion of the source body is expressed in terms of the Doppler amplification factor $(1/(1 - M_r))$. The sound waves are accumulated in the direction of motion (but spread out behind the moving body), resulting in the amplification of frequency and amplitude by the Doppler factor [6].

For a body in subsonic motion, there is only one emission time τ_e (for a given source panel at emission position $y_e = y(\eta, \tau_e)$ and emission distance r_e) for the observer position x and the observer time t [28]. These relative characteristics can be computed through retarded time formulation from

$$(2.7) \qquad \tau - t + \frac{|x - y(\eta, \tau)|}{c_0} = 0.$$

3. Methodology

3.1. Source generation: BEMT in-house code

To predict loading noise the distribution of loads on the blade surface is required [10]. The surface forces may be estimated with simpler, engineering methods, such as the BEMT or directly computed using more advanced CFD solvers. The BEMT method is known to be fast, but also less accurate than CFD. However, it is included in the analysis, because it is applied for comparison purposes of the developed code and the reference FW–H code. Two model rotors are investigated in the paper: Caradonna–Tung (C–T) [35] and Sargent–Schmitz (S–S) [30], all operating in low-thrust hover conditions and equipped with blades of rectangular planform and NACA 0012 section. Unfortunately, blade loading is not provided for the experiment selected for the investigation of the prediction capabilities of the developed FW–H solver (S–S rotor), therefore the C–T rotor is included to complete the validation of the methodology in terms of the aerodynamic performance. Later, the same BEMT and CFD modeling is applied for an acoustic analysis of S–S rotor (noise generation and propagation), for which no aerodynamic data is available.

BEMT is a hybrid method, combining the blade element and the momentum theories, that is designed for rotary wing analysis [36]. It is able to predict rotor loading, depending on: the number of blades, the blade radius and shape (airfoil type, twist, and taper distributions, etc.), the operating conditions, and the induced inflow model (non-uniform inflow with the Prandtl tip-loss function). The sectional lift c_l and drag c_d coefficients are assumed to be known though, e.g. from a separate 2d analysis (experimental or numerical). As a result the rotor thrust c_t and torque c_q coefficients as well as the blade radial distribution of in-plane and out-of-plane components of the aerodynamic force are obtained, which may be directly used as an input to the FW–H solver for acoustic predictions of rotor loading noise. The compact chord form of this loading is applied at $0.25\,c$ along the blade span. The simplest approach is to assume that the lift curve slope is equal to $c_{l\alpha} = 2\pi$ and the drag coefficient is constant regardless of the angle of attack α (e.g. $c_d = c_{d0} = 0.015$), as in [30]. This assumption is justified by the low collective pitch angle θ setting of the blades for all investigated rotors.

3.2. Source generation: CFD solver FLOWer (DLR)

The CFD solver FLOWer is developed by the German Aerospace Center (DLR) and extensively used by German research organizations, universities, and aerospace industry (e.g. Airbus) [37]. It is an aviation oriented tool that solves numerically compressible, Favre-averaged mass, momentum, and energy conservation equations with various low-Reynolds 1- and 2-equation eddy-viscosity

turbulence models (e.g. Linear Explicit Algebraic LEA $k - \Omega$ [38]) on multiblock structured grids. The ROT version of the code is designed specifically for simulation of flows past moving bodies, such as rotating helicopter rotor blades in hover or a forward flight. The classical semi-discrete algorithm is based on the finite volume method for spatial discretization (2nd order). For approximation of convective and diffusive fluxes the central scheme with scalar artificial dissipation is implemented. The implicit dual-time-stepping approach is used for integration in time (2nd order). Internal iterations in pseudo-time are progressed with the explicit Runge–Kutta method, supplemented by the convergence acceleration techniques, i.e. multigrid, local time-stepping, and implicit residual smoothing. The flow equations are solved in the absolute reference frame, therefore the rotation of the rotor blades is imposed as the circulation of the entire computational domain (unsteady approach).

3.3. Source propagation: Elementary sources

For purpose of verification and validation of the developed FW–H code, presented in Section 2.1 analytical solutions (Eqs. (2.2) and (2.3)) of acoustic radiation of elementary monopole and dipole point sources are utilized. The thickness noise is modeled as a rotating pair of source and sink of mass, while the dipole as a rotating source of momentum (force). The estimation of the involved variables (e.g. the Mach number of the source towards the observer, M_r) are proceeded in a similar fashion to the FW–H code. Since even the analytical sources must be discretized to perform necessary comparisons, the impact of the number of samples is limited by taking a sufficiently small time-step Δt (i.e. $\Delta t = T/10000$, T – period of rotation). Moreover, it is assured that the signal length is sufficient for meaningfull DFFT of acoustic pressure. All presented solutions (analytical) for elementary cases are computed with $\Delta t = T/10000$ and for at least 2.5 periods T of rotation.

In general, the prediction of loading noise based on CFD results (blade pressure) is time-consuming. Therefore, a simplified code is developed for numerical analysis of distributed sources (such as rotating helicopter or wind turbine blades) based on derived analytical solutions for a moving point force. This way, the BEMT loading distribution is applied along the span at quarter chord of the blade (so-called compact chord assumption). The total acoustic pressure is then obtained by linearly summing up the signals originating from each section at the correct observer time. With such approach the loading noise is efficiently predicted at a fraction of the effort of the full CFD + FW–H analysis. The presented analytical solution for dipole is not only used for the FW–H code validation but also for the initial assessment of the loading noise of rotating bodies (distributed sources). The assessment of both approaches (analytical and FW–H) is quantified in Section 6.3 for the S–S rotor in hover.

3.4. Source propagation: FW–H code

An in-house aeroacoustic code based on Farassat's Formulation 1A (Section 2.2) is developed using the macro language directives of Tecplot 360 EX – a popular commercial post-processing software. Since Tecplot 360 EX offers input filters for a variety of non-commercial and commercial CFD solvers, the FW–H aeroacoustic analysis may be executed efficiently not only for new computational projects and included in the work-flow, but also conducted directly for already existing numerical data (e.g. RANS). Moreover, Tecplot 360 EX improves greatly the handling of complex geometries and large computational grids, providing numerous benefits in terms of specialized functions utilized by the code (e.g. cell metrics calculation or DFFT (Discrete Fast Fourier Transform) of acoustic pressure signals). Aforementioned features are valuable and constituted a major driver for initial code development.

For an acoustic analysis a discretized model of the source (i.e. surface mesh) is required. For the acoustic analysis of complex rotating bodies (such as helicopter rotor blades), the CFD grid is used directly. The source surface definition and kinematics constitute the input for thickness and loading noise prediction modules. Additionaly, the surface pressure distribution is necessary for loading noise estimation (e.g. from BEMT or CFD). Each surface mesh cell is treated as a separate acoustic source panel (Fig. 1) for which the acoustic potential (i.e. integrands in Eqs. (2.5) and (2.6)) are evaluated in time.
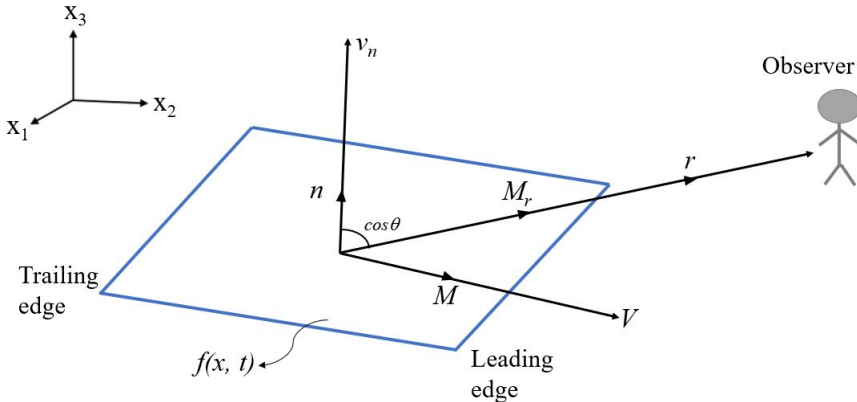

Fig. 1. Sketch of a single acoustic source panel.

If multi-block grids are exploited by the numerical simulations (CFD), the consecutive mesh blocks can be analysed together as a set or individually fed to the acoustic code, allowing for serial or parallel runs. Initially, the code computes all the variables of Farassat's Formulation 1A (Eqs. (2.5) and (2.6)) and stores

the acoustic potential of every panel at the emission time (τ). The contribution of a single panel depends on its initial position (orientation in space) and motion in relation to the observer which are not affected by the neighbouring acoustic panel's presence. Such features provide flexibility in identification of specific components (e.g. root, tip, and tip cap for a rotor blade, etc.) or add-ons (e.g. vortex generators), to assess their acoustic impact.

There are numerous retarded time algorithms designed for evaluation of Farassat's Formulation 1A integrals, such as source-time dominant, mid-panel and high accuracy quadratures, or supersonic source motion [10]. The source-time dominant method is implemented in the FW–H code, since it is numerically simple (non-iterative) and relatively easy to interpret. All the variables are evaluated at the source retarded (emission) time. The primary application of the developed FW–H code is the acoustic analysis of rotating blades for stationary observers. Thus the corresponding observer time (t) is computed for every acoustic panel at each emission time-step using the retarded time relation (Eq. (2.7)). Finally, the multiple source contributions at the correct observer time are added together to obtain the total acoustic pressure signal at a listener position. For numerical time differentiation the fourth-order schemes have been implemented [39], while, for surface integrals a second order mid-panel approximation is used. It is important to emphasize that the final noise signature recorded at a given observer location depends not only on the strength of the sources, but is also affected by cancellation/amplification effects due to variability of the reception time of acoustic panels (distributed sources).

4. Validation of the FW–H code (elementary point sources)

The accuracy of the developed FW–H code is validated against analytical solutions (discretized Eqs. (2.2) and (2.3)) derived for elementary moving acoustic sources. The rotating point source of mass (monopole) is modeled as a sphere of finite (small) radius with the constant mass-flux. The topology of the structured multi-block mesh of the sphere surface contains 6 blocks and is designed using Interactive Grid Generator (IGG) from Numeca International (Fig. 2). Each of the 6 component blocks contains 16×16 (256) cells (acoustic panels). The mesh convergence study is conducted with coarse, medium and fine grids, in total consisting of 96, 384, and 1536 cells, each one 4 times finer than the coarser one (2 times in each direction). Analogously, the rotating point source of momentum (dipole) is modelled as a disc of finite (small) radius with an applied constant force. The topology of the structured multi-block grid of the disc surface contains 5 blocks (IGG) – Fig. 6. Each of the 5 component blocks contains 16×16 (256) cells. Also here the mesh convergence study is conducted with coarse, medium and fine grids, in total consisting of 80, 320, and 1280 cells.

The chosen dimensions are compatible between rotating monopole and dipole cases, since the number of acoustic panels per unit surface area of the source is constant for each level, i.e. coarse, medium, and fine. Additionaly, a source size dependency analysis is performed for both, the sphere and the disc of radii 0.025 m, 0.0125 m, 0.00625 m (relative factor of 2). Finally, the time-step convergence study is proceeded for 180 (coarse), 360 (medium), 720 (fine) and 5760 (very fine) samples per period of rotation T. The resultant signals (analytical and predicted) for all cases are analyzed in time and frequency domains and compared in terms of the peak amplitude and the root-mean square of pressure fluctuations (p_{rms}), dominant frequency, Sound Pressure Level (SPL) spectrum, and the Overall Sound Pressure Level (OASPL).

In the time domain analysis, p_{rms} is defined as the root mean square of the acoustic pressure fluctuations expressed as Eq. 4.1 with $p'(t)$ being the pressure at time t [19, 29]

$$(4.1) \qquad p_{rms} = \sqrt{\frac{1}{T_2 - T_1} \int_{T_1}^{T_2} p'(t)^2 \, dt}.$$

The OASPL is given by Eq. (4.2) with P_{ref} as the reference pressure [29]

$$(4.2) \qquad \text{OASPL} = 10 \log_{10}\left(\frac{p_{rms}^2}{P_{ref}^2}\right).$$

Applying DFFT to the acoustic pressure signal to obtain frequency, SPL is computed using Eq. (4.3)

$$(4.3) \qquad \text{SPL} = 10 \log_{10}\left(\frac{L}{2N^2} \frac{f_A^2}{P_{ref}^2}\right),$$

where N is the number of samples in the total time of analysis L and f_A is the amplitude of source fluctuations at a given frequency.

The OASPL can also be computed from a frequency analysis using Eq. (4.4)

$$(4.4) \qquad \text{OASPL} = 10 \log_{10}\left(\int_0^\infty 10^{0.1(SPL)} \, df\right).$$

The spatial and temporal resolution and source size dependency investigations are continued until the relative error (difference between analytical and predicted FW–H code values divided by the reference analytical one) is less than 0.5% for all depicted noise metrics (accuracy measure). However, due to space limitations, only final solutions are presented here.

4.1. Case 1: rotating source/sink of mass (monopole)

The rotating source/sink of mass case is designed specifically to mimic thickness noise pulse (large negative peak surrounded by two smaller positive humps) generation mechanism (monopole) and is described in detail by Schmitz in [6] for a helicopter rotor radiation. The tip of the rotor blade (the most efficient source of thickness noise) is modelled as an equivalent body in motion. It consists of two small radius spheres subjected to the surface mass transfer and positioned equivalently to leading (source) and trailing (sink) edges of the airfoil (Fig. 2). It is the time delay in receiving the pulses emitted by the source and by the sink at the far-field observer location that is responsible for the the recorded acoustic pressure signal.
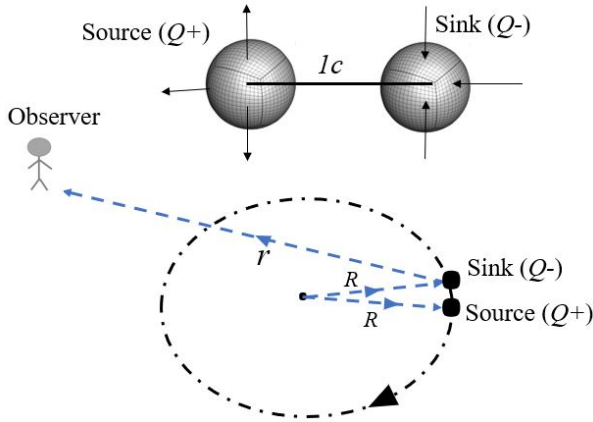
Fig. 2. Rotating source/sink of mass – model of thickness (monopole) noise radiation.

Two spheres of the same size are placed at a relative distance equal to the chord length ($c = 0.1$ m) of the Sargent–Schmitz helicopter rotor blade investigated in Section 6. Moreover, the rotation arm ($R = 1$ m), the rotation frequency ($f_{rot} = 36$ Hz) are also replicated and the ambient conditions are $P_0 = 103630$ Pa and $T_0 = 288.15$ K. The mass flow rates of the source and of the sink are equal in strength $q = 0.1$ kg/s but opposite in terms of direction (sign). Since the far-field acoustic signatures are of major concern, a stationary observer is placed at a distance of 8 m ($8R$) from the centre and in the rotation plane. The FW–H code acoustic prediction is compared with the analytical solution (Eq. (2.2)), first in terms of the near- and the far-field components (and the total signal) of the source and of the sink separately. Finally, a combined acoustic presure pulse of the rotating source/sink pair is presented (in time and frequency domains) resembling in many details the thickness noise signal shape radiated in-plane by a helicopter rotor blade.

As a result of sphere size, grid, and time-step dependency studies (see more details in Appendix), the spheres of radii of 0.00625 m, the surface grid of 1536 source panels, and the time-step of $T/5760$ ($T = 27$ ms – period of rotation) are chosen for further acoustic analysis. The FW–H solution error is below 0.5% for almost all depicted noise metrics (amplitude, p_{rms}, frequency, and OASPL). The rotating source and the rotating sink acoustic pressure signals are of opposite nature (and slightly delayed in relation to each other), i.e. the source emits a positive peak followed by a negative peak, while the sink radiates the inverse pattern (Fig. 3). For the chosen in-plane observer location, the far-field
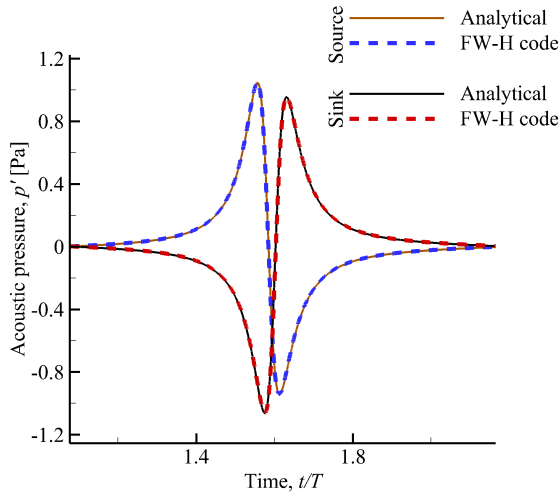

Fig. 3. Total acoustic pressure (p') signals for a rotating source and a rotating sink.

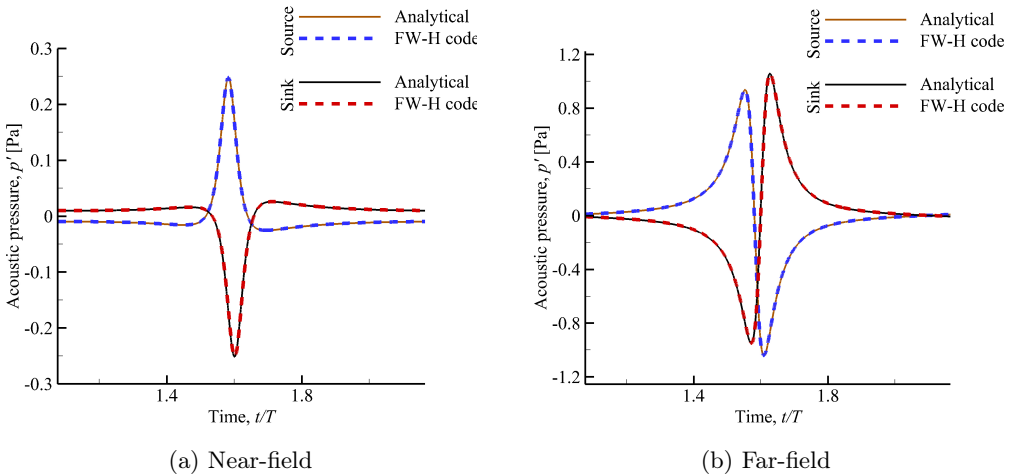(a) Near-field   (b) Far-field

Fig. 4. Acoustic pressure (p') signal components for a rotating source and a rotating sink.

component of the acoustic pulse is predominant over the near-field one (Fig. 4). The evident shift in the observer time for both acoustic sources prevents the two signals from cancelling out each other completely (which is exactly the case for an observer located on the rotation axis) [7]. The FW–H code predictions of the total acoustic signal, split into near-field and far-field terms, are in good agreement with the analytical solutions (Figs. 3, 4).

The acoustic signals emitted by the source and by the sink are now added together at the correct observer time to obtain the combined noise pulse shape (Fig. 5). For an in-plane observer location, due to the existence of the time delay between the maximum acoustic emission of the source and of the sink (separated in space), the resultant pulse width is very narrow and constitutes only a fraction of the rotation period T (approximately 2.25 ms, i.e. 30° of rotation). The basic characteristics of this signal are similar to the thickness noise that is generated as a consequence of the displacement of mass of fluid by the movement of rotating bodies in space (e.g. propeller or helicopter rotor blades). Because the ambient conditions (and speed of sound) are considered as constant, the radiation mechanism of the symmetrical negative peak followed by two smaller positive humps is governed mainly by the projection of the normal velocity v_n at each acoustic panel on the radiation vector connecting the source and the observer r (integrated over the source area). For the considered case the v_n velocity consists of two separate components, i.e. due to surface rotation and mass transfer. The FW–H code prediction of the combined acoustic signal of source-sink pair is also in good agreement with the analytical solution for both, the time (Fig. 5a) and the frequency (Fig. 5b) domains. As expected, the acoustic spectra are dominated by low frequencies (maximum at approx.
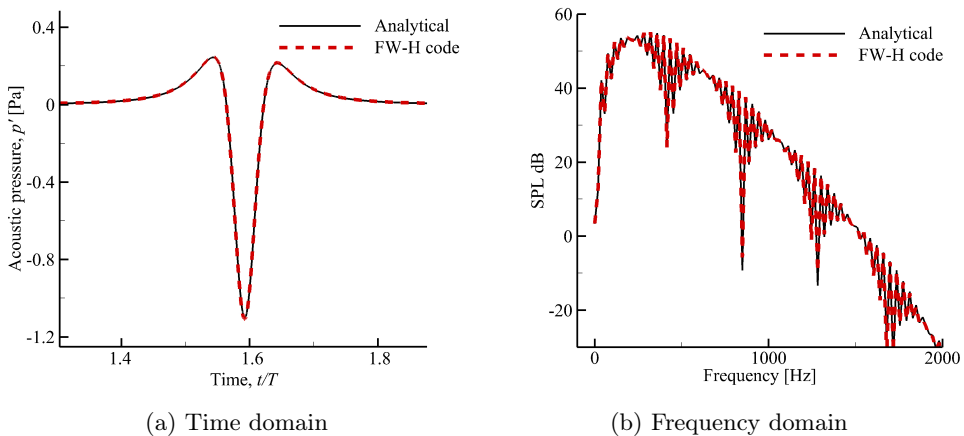

(a) Time domain   (b) Frequency domain

Fig. 5. Addition of total acoustic pressure emitted by rotating source-sink pair.

250 Hz), with significant emission taking place in the bass and midrange bands (up to 1 kHz).

A more detailed evaluation of the FW–H code accuracy in relation to the analytical solutions is presented in Tables 1 and 2 for the individual source and sink, as well as for the combined source-sink pair cases. The amplitude (1 Pa), the root-mean-square of pressure fluctuations p_{rms} (0.3 Pa), the frequency of the first harmonic (36 Hz) and the OASPL (84 dB) of separate source and sink signals are practically equal. When both sources are radiating (source and sink), a partial cancellation effect takes place, i.e. OASPL is reduced by 5 dB. It is worth to notice that 6 dB difference in OASPL signifies two times lower p_{rms}. Due to the thickness noise generation mechanism, the combined (source+sink) pulse shape analysis is very sensitive to the time-step size choice, therefore is more difficult to predict. Still, the relative error for all presented cases and parameters is below 0.7%, which validates the FW–H code functionality in terms of the monopole radiation. Moreover, an important verification is that the OASPL values computed from time signals (p_{rms}) and obtained by integration of SPL spectra are equal within 0.3 dB accuracy.

Table 1. Time domain analysis for a rotating source, sink and a source-sink pair.

Monopole	Code	Amplitude [Pa]	Error %	p_{rms} [Pa]	Error %	OASPL dB	Error dB
Source	Analytical	1.046	—	0.313	—	83.879	—
	FW–H	1.045	0.095	0.312	0.102	83.870	0.009
Sink	Analytical	0.955	—	0.316	—	83.966	—
	FW–H	0.954	0.094	0.315	0.151	83.957	0.009
Source + Sink	Analytical	−1.100	—	0.1767	—	78.920	—
	FW–H	−1.108	-0.699	0.1767	0.005	79.072	−0.152

Table 2. Frequency domain analysis for a rotating source, sink and source-sink pair.

Monopole	Code	Frequency [Hz]	Error %	OASPL dB	Error dB
Source	Analytical	36.082	—	83.87	—
	FW–H	36.083	−0.002	83.65	0.22
Sink	Analytical	36.081	—	83.83	—
	FW–H	36.083	−0.005	83.74	0.09
Source + Sink	Analytical	37.47	—	78.71	—
	FW–H	37.48	−0.026	78.77	−0.06

4.2. Case 2: rotating force (dipole)

The rotating force case is designed specifically to mimic loading noise generation mechanism (dipole) for a helicopter rotor radiation. Again, the tip of the rotor blade (the most efficient source of loading noise) is modelled as an equivalent body in motion. It consists of a small radius disc subjected to a force of constant magnitude (out-of-plane/in-plane) and positioned at the quarter chord of the airfoil (Fig. 6). The magnitude of the force (100 N) is assured by proper surface pressure distribution (uniform), while the force direction is always perpendicular to the rotating disk. For the out-of-plane force acting on a rotating body, the disc is kept parallel to the rotation plane (XY) and the force components $(0, 0, 100$ N$)$ do not change in time (Fig. 6a). This set-up is analogous to the thrust (axial) force acting on the rotor blades. However, for the rotating in-plane force case, the disc orientation and the force direction are varying in time (Fig. 6b), although the force magnitude remains constant. For a helicopter rotor the in-plane force is responsible for shaft torque generation. The rotation arm is R $= 1$ m, with $f_{rot} = 36$ Hz, $P_0 = 101325$ Pa and $T_0 = 288$ K. Since the far-field acoustic signatures are of major concern, stationary observers are placed 8 m above the rotation plane $(1, 0, 8)$ and 8 m from the rotation centre $(8, 0, 0)$ for the out-of-plane and in-plane force cases, respectively. The rotating radial force case was also analysed but is not presented due to rather low impact on the acoustic signature of the rotor.
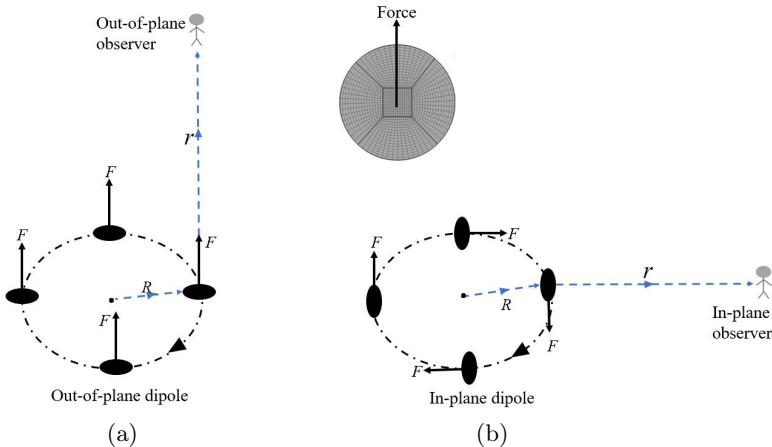

(a) (b)

Fig. 6. Rotating force – model of loading (dipole) noise radiation.

As a result of disc size, grid, and time-step dependency studies (see more details in Appendix), the disc radius of 0.00625 m, the surface grid of 1280 source panels, and the time-step of $T/720$ ($T = 27$ ms – period of rotation) are chosen for the further acoustic analysis. The FW–H solution error is below 0.5% for all

depicted noise metrics (amplitude, p_{rms}, frequency, and OASPL). However, for an improved comparison of the SPL spectra with analytical solutions and for consistency with the monopole radiation model case, a much finer time-step of $T/5760$ is assumed for all subsequent plots.

The FW–H code acoustic prediction is compared with the analytical solution (Eq. (2.3)), first in terms of the near- and far-field components (and the total signal), as well as for the sound pressure level (SPL) spectrum for the rotating out-of-plane force case (Fig. 7). Both the near- and far-field components of the acoustic pressure pulse are of similar nature (almost harmonic), only slightly delayed in relation to each other (nearly in-phase) – see Figs. 7a, 7b. For the chosen out-of-plane observer location, the far-field component of the signal is predominant over the near-field one. The FW–H code predictions of the total
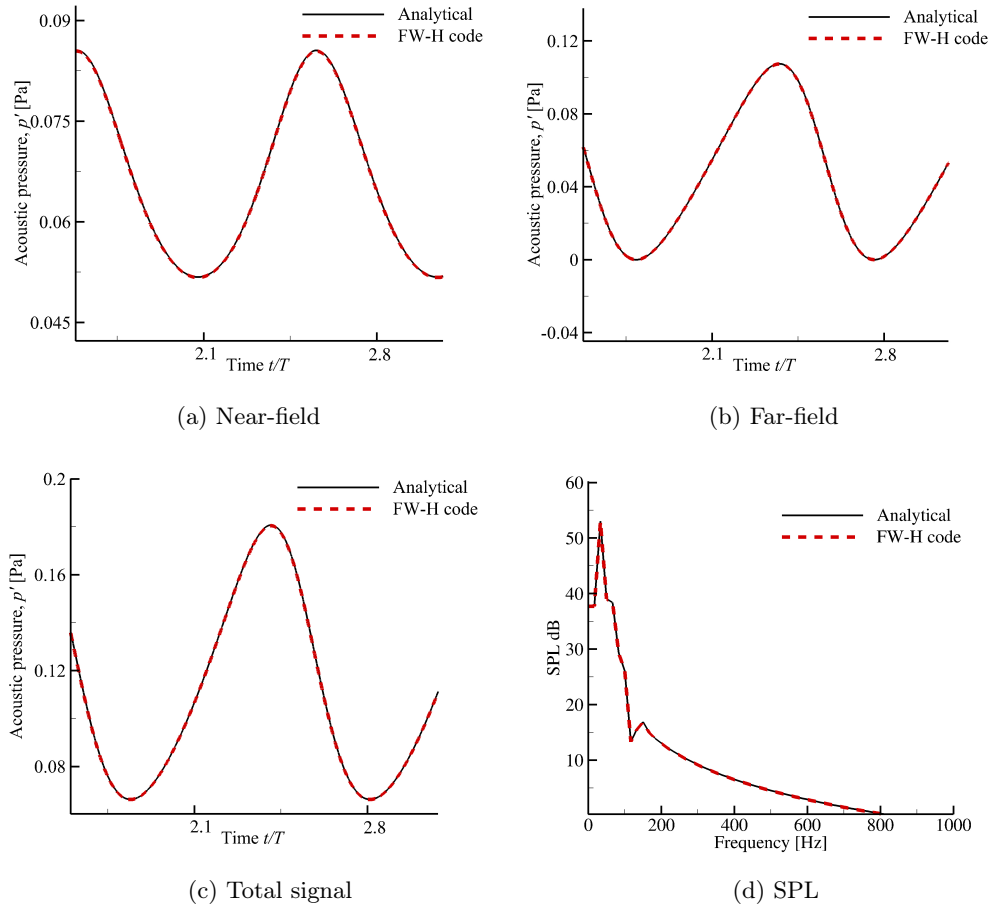

(a) Near-field

(b) Far-field

(c) Total signal

(d) SPL

FIG. 7. Acoustic pressure (p') signal components and SPL for a rotating out-of-plane force.

acoustic signal (Fig. 7c) and its components are in good agreement with the
analytical solutions in both time and frequency domains.

The total acoustic presure pulse comparison for the rotating in-plane force
case is presented in Fig. 8. Again, the FW–H code prediction is in satisfactory
agreement with the analytical solution, both qualitatively and quantitatively, for
time (Fig. 8a) and spectral (Fig. 8b) analyses. Despite the equal force magnitude
(100 N), rotation arm (1 m), and frequency (36 Hz) and similar distance between
the rotation centre and the observer location, the amplitude of the signal emitted
due to the in-plane force is much higher than due to the out-of-plane force. Such
a feature is not only a consequence of the force vector acting in the direction
tangent to the rotation plane (therefore its components significantly varying in
time), but also of the in-plane observer position (maximum acoustic radiation).
As expected, the acoustic spectra are dominated by low frequencies (maximum at
approx. 100 Hz), with significant emission taking place in the bass and midrange
bands (up to 1 kHz). As is presented in Section 6.3, apart from the dominating
thickness (monopole) component, both the out-of-plane and the in-plane forces
acting on the rotor blades do contribute to the final amplitude and shape of the
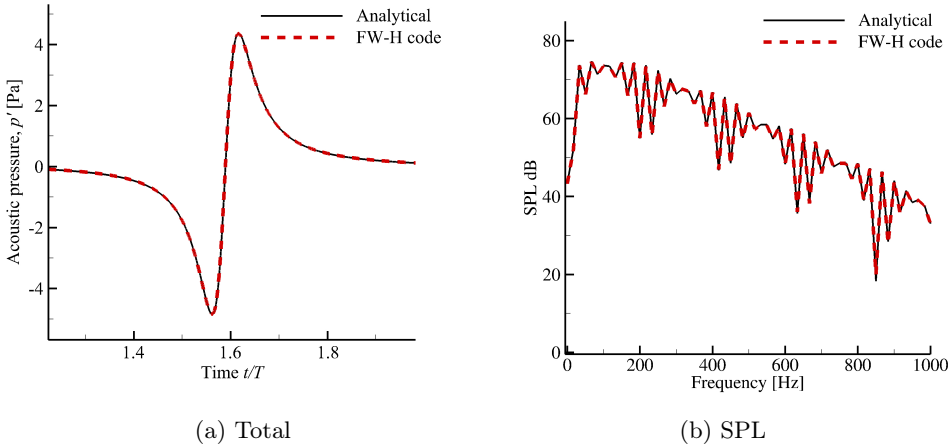acoustic signal of the LF-IPH noise.

(a) Total   (b) SPL

FIG. 8. Acoustic pressure (p') signal components and SPL for a rotating in-plane force.

The FW–H code prediction is in good agreement with the analytical solution
both qualitatively and quantitatively. The sound emitted by the in-plane force
has a peak amplitude of ∼4 Pa. The signal has a large amplitude compared
to the out-of-plane dipole due to equal strength of force applied (100 N) and
the chosen observer location. The observer locations are chosen to have all the
variables active and contributing to the acoustic potential.

A more detailed evaluation of the FW–H code accuracy in relation to the analytical solutions is presented in Tables 3 and 4 for the rotating out-of-plane and in-plane force cases. As mentioned before, the amplitude, the p_{rms} and the OASPL differ by 1-2 orders of magnitude between both sources (delta of 21 decibel). Still, the frequencies of the first harmonics are equal (36 Hz). The relative error for all presented cases and depicted parameters is below 0.5%, which validates the FW–H code functionality in terms of the dipole radiation. Moreover, an important verification is that the OASPL values computed from time signals (p_{rms}) and obtained by integration of SPL spectra are within 0.4 decibel accuracy.

Table 3. Time domain analysis for a rotating out-of-plane and in-plane forces.

Dipole	Code	Amplitude [Pa]	Error %	p_{rms} [Pa]	Error %	OASPL dB	Error dB
Out-of-plane	Analytical	0.1807	–	0.1233	–	75.80	–
	FW–H	0.1804	0.16	0.1229	0.33	75.78	0.02
In-plane	Analytical	4.36	–	1.414	–	96.99	–
	FW–H	4.35	0.22	1.412	0.15	96.98	0.01

Table 4. Frequency domain analysis for a rotating out-of-plane and in-plane forces.

Dipole	Code	Frequency [Hz]	Error %	OASPL dB	Error dB
Out-of-plane	Analytical	36.364	–	75.78	–
	FW–H	36.365	−0.002	75.76	0.02
In-plane	Analytical	36.367	–	96.96	–
	FW–H	36.365	0.005	97.00	−0.05

5. Validation of the source generation methods: BEMT and CFD

5.1. 2-bladed C–T model rotor geometry

The rotor consists of 2 untwisted, untapered and rigid blades having a rectangular planform and NACA 0012 symmetrical cross-section [35]. The chord length is constant and equal to $c = 0.1905$ m, while the blade radius is $R = 1.143$ m (the aspect ratio of $AR = 6$). Various tip Mach numbers ($M_T = 0.23 \ldots 0.89$) and blade collective pitch angles ($\theta = 0° \ldots 12°$) were investigated. The pressure coefficient c_p distributions were measured at 5 cross-sections. Spanwise blade loading (the sectional lift coefficient c_l) and the integrated rotor thrust coefficient c_t were estimated based on the surface pressure values at discrete radial positions.
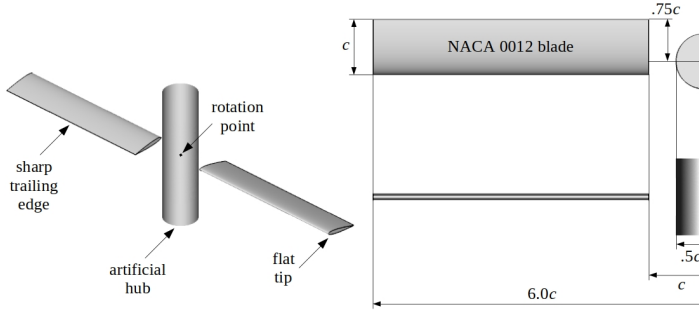
Fig. 9. C–T model rotor geometry and dimensions.

The computational model of the C–T rotor consists of 2 blades and the artificial hub surface (see Fig. 9). Keeping the aspect ratio constant ($AR = 6$), the geometry is up-scaled to chord length $c = 1$ (radius $R = 6$). The radius of the artificial hub is $0.5\,c$, while the inner part of the blade is removed and the blade root is located at $1.0\,c$. No information is provided regarding the tip or the root cut-off shapes, so flat surfaces are applied. The blade trailing edge is sharp (zero thickness) and the pitch axis is set to $0.25\,c$.

5.2. Numerical model description

The generation of the multi-block structured computational mesh is automated and processed with in-house software developed for two investigated configurations (C–T and S–S rotors) using Python programming language and IGG from Numeca International. The computational domain consists of 160 blocks (80 blocks per blade), with C–topology in streamwise and H-topology in normal and spanwise directions (Fig. 10). The C–H–H topology proves to be effective in
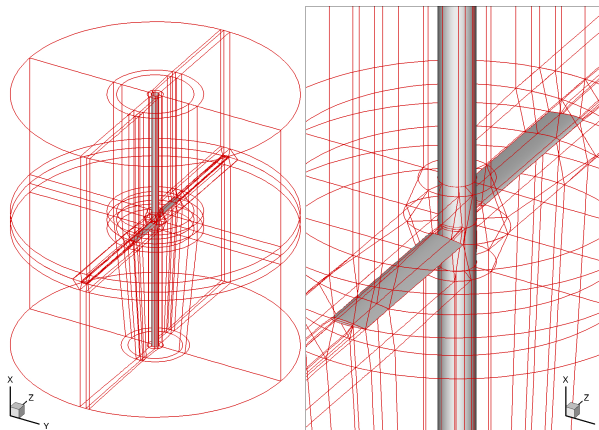

Fig. 10. Multi-block structured C–H–H grid topology (160 blocks).

capturing the rotor induced inflow velocity and wake system. The computational grid contains $11.39 \cdot 10^6$ of control volumes ($5.70 \cdot 10^6$ per blade) (see Fig. 11). The mesh points are clustered in boundary layers and in the wake, especially near the blade tip and tip vortex locations. Since a low-Re number turbulence model is used, the non-dimensional distance of the first mesh point from the surface is set to be of the order of 1. In total 88% of cells exhibit the most desired orthogonality level (75°–90°), with additional 8% in the range 60°–75°. Due to the adopted topology, the remaining 4% of lower quality cells cannot be improved (because of their location near the sharp trailing edge-flat tip cap corner). The maximum aspect ratio is 5850, with the most elongated control volumes located near the outer edge of the computational domain. To visualize the volume mesh setup, Fig. 11 depicts in yellow, two exemplary cross-sections (chordwise and spanwise), presenting computational grid arrangement near the rotor plane.
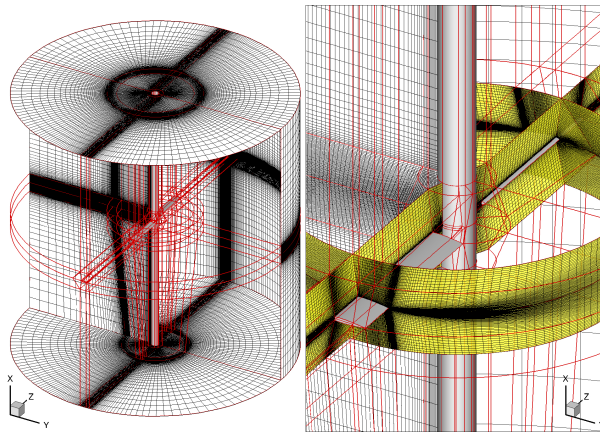

Fig. 11. Multi-block structured C–H–H grid ($11.39 \cdot 10^6$ of volumes).

The computational set-up is based on 3 types of boundary conditions, applied at the outer surface of the computational domain, artificial hub and blade surfaces (Fig. 12). The blade surface is modeled with the viscous (no-slip) adiabatic wall boundary condition (red color in Fig. 12). In contrast, to save computational resources the artificial hub surface is simplified by the inviscid (slip) adiabatic wall boundary condition (green color in Fig. 12). Even though this flow is periodic in nature, the entire rotor is simulated (2 blades) without the rotational periodicity condition. For the outer edge of the computational domain (rotation in each direction), the Freude source-sink boundary condition is applied, designed specifically for helicopter rotors in hover (black and blue colors in Fig. 12). It is an extension of the characteristic variable far-field boundary condition that
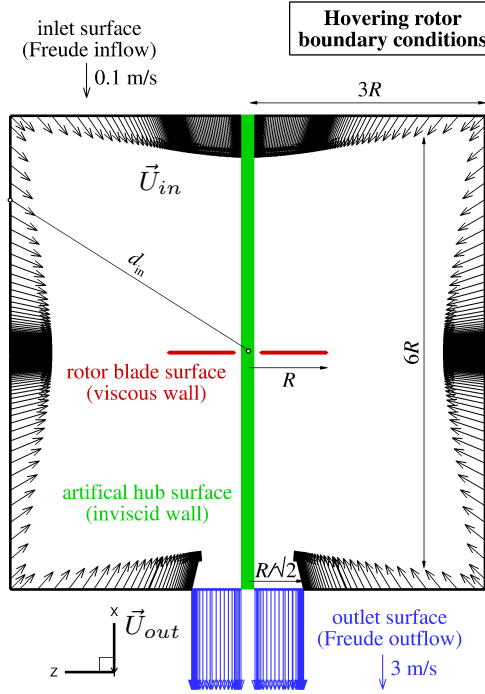
Fig. 12. Computational domain and boundary conditions.

Table 5. C–T model rotor dimensions and operating conditions.

Parameter	Experiment	CFD
Rotor radius, R [m]	1.143	6.0
Blade chord length, c [m]	0.1905	1.0
Rotor aspect ratio, AR	6.0	6.0
Blade collective angle, θ [°]	2.0	2.0
Ambient pressure, P_0 [Pa]	101325	19250
Ambient temperature, T_0 [K]	290.2	290.2
Ambient density, ρ_0 [kg/m^3]	1.22	0.232
Ambient viscosity, μ_0 [Pa·s]	$1.8 \cdot 10^{-5}$	$1.8 \cdot 10^{-5}$
Ambient speed of sound, c_0 [m/s]	341.5	341.5
Rotational speed, RPM	2265	431.5
Tip Mach number, M_T	0.794	0.794
Tip Reynolds number, Re_T	$3.5 \cdot 10^6$	$3.5 \cdot 10^6$
Tip velocity, V_T [m/s]	271.1	271.1
Frequency of rotation, f_{rot} [Hz]	37.75	7.191
Period of rotation, T [ms]	26.5	139

is taking into account the induced velocities caused by the downwash of the rotor [40]. This approach is meant to limit the impact of the choice of the domain dimensions on the predicted rotor performance, therefore not only significantly reducing the computational effort, but also causing the domain size dependency tests to be unnecessary.

The rotor is positioned in a quiescent medium with ambient temperature T_0 and pressure P_0 (Table 5). A non-zero velocity is induced at the boundaries, if the blades are rotating with the collective pitch θ set to a positive value. Air is drawn into the computational domain, towards the rotation center, with velocity $\vec{U}_{in}$ calculation based on the momentum theory (Freude inflow):

$$(5.1) \qquad \vec{U}_{in} = \frac{A_{rotor}}{4\pi d_{in}^2} \sqrt{\frac{F_T}{2\rho_0 A_{rotor}}} \widehat{e}_{in},$$

where A_{rotor} – rotor disc area (πR^2), d_{in} – distance from the rotation center, F_T – rotor thrust force, ρ_0 – ambient density, and $\widehat{e}_{in}$ – unit vector pointing towards the rotation center. The outlet is imposed only at a small circle, just below the rotor disc, with radius of $R/\sqrt{2}$ (Freude outflow), where air is leaving the computational domain with constant velocity vector $\vec{U}_{out}$:

$$(5.2) \qquad \vec{U}_{out} = 2\sqrt{\frac{F_T}{2\rho_0 A_{rotor}}} \widehat{e}_{out},$$

where $\widehat{e}_{out}$ symbolizes a unit vector pointing in the opposite direction to rotation centre.

For validation of the FLOWer code applied to a hovering helicopter rotor of C–T, a low-thrust case is selected with collective pitch setting $\theta = 2°$, compatible with S–S rotor investigation (also $\theta = 2°$). The ambient temperature $T_0 = 290.2$ K is derived from M_T and rotor RPM, while the unknown ambient pressure P_0 is fixed at 101325 Pa (Standard Day Conditions). Re-scaling of the blade chord to $c = 1$ necessitates a modification to the rotor operating conditions (see Table 5). Keeping M_T and Re_T, as well as the tip velocity V_T and T_0 constant, the ambient pressure P_0 and density ρ_0 are affected, accompanied by reduction of the frequency of rotation. Additionally, the two-equation LEA $k - \Omega$ closure requires specification of the inlet turbulence parameters, which are not provided, therefore the FLOWer default values of the eddy viscosity ratio of 0.001 (ratio of turbulent eddy viscosity to molecular dynamic viscosity) and of the turbulence level of 0.5% are adopted. The temporal accuracy of the presented solution is assured by the choice of a sufficiently small time-step Δt of the numerical scheme, corresponding to 0.25° of rotation (i.e. $\Delta t = 9.66 \cdot 10^{-5}$s), giving 1440 time-steps per revolution. A similar computational model has been

already validated and applied during previous research regarding aerodynamics and aeroacoustics of helicopter rotors, with the FLOWer [41], Fine/Turbo (Numeca International), Fluent (Ansys) and SPARC (University of Karlsruhe) solvers.

5.3. Grid and time-step dependency studies

The examination of the spatial and temporal convergence of CFD results is a straight-forward method for determining the discretization error. As the grid or the time-step are refined, the spatial and temporal discretization errors should asymptotically approach zero. The Grid Convergence Index (GCI) approach, described by Roache in [42], is applied for total forces of the rotor. The mean rotor thrust c_t and torque c_q coefficients (pressure and friction), based on the thrust force F_T [N] and shaft torque F_Q [Nm], are defined by

$$(5.3) \qquad c_t = \frac{F_T}{\rho_0 V_T^2 A_{rotor}}, \qquad c_q = \frac{F_Q}{\rho_0 V_T^2 A_{rotor} R}.$$

The simulations of the C–T rotor flow-field are performed on a sequence of grids (with medium time-step): coarse ($1.42 \cdot 10^6$ volumes), medium ($11.39 \cdot 10^6$ volumes) and fine ($91.10 \cdot 10^6$ volumes), every mesh being 8-times finer than the coarser one (i.e. refined twice in each direction), therefore marked as cell sizes of: "4", "2", and "1", respectively (Table 6). For a temporal accuracy convergence study (on medium grid), three values for time-step (Δt) size are investigated: coarse ($0.5°/720$ per revolution), medium ($0.25°/1440$ per revolution) and fine ($0.125°/2880$ per revolution), designated as time-step sizes of: "4", "2", and "1", respectively (Table 7). The solutions obtained by Richardson's extrapolation are provided in Tables 6 and 7 as well, and numbered as the cell size of "0" (infinite number of volumes) and the time-step size of "0°" (infinite number of time-steps per period or rotation). The obtained rotor thrust and torque coefficients exhibit asymptotic behavior, while the grid and time-step are successively refined (see Figs. 13a and 13b).

Table 6. Grid dependency study – averaged rotor thrust and torque coefficients ($M_T = 0.794$, $\mathrm{Re}_T = 3.5 \cdot 10^6$, **and** $\theta = 2°$) **(medium time-step of** $0.25°$**).**

Spatial	Number of volumes	Cell size	c_t $\cdot 10^{-4}$	c_q $\cdot 10^{-4}$	$\Delta_1(c_t/c_q)$ %	$\Delta_0(c_t/c_q)$ %	GCI_{2-0} (c_t/c_q) %	GCI_{1-0} (c_t/c_q) %
Coarse	$1.42 \cdot 10^6$	4	5.262	1.368	9.5/4.1	10.0/4.1	n.a.	n.a.
Medium	$11.39 \cdot 10^6$	**2**	**5.711**	**1.426**	**1.8/0.1**	**2.3/0.1**	**3.0/0.1**	**n.a.**
Fine	$91.10 \cdot 10^6$	1	5.815	1.427	0/0	0.5/<0.1	n.a.	0.7/<0.1
Extrapolated	∞	0	5.846	1.427	n.a.	0/0	n.a.	n.a.

Table 7. Time-step dependency study – averaged rotor thrust and torque coefficients ($M_T = 0.794$, $\mathrm{Re}_T = 3.5 \cdot 10^6$, and $\theta = 2°$) (medium grid of $11.39 \cdot 10^6$).
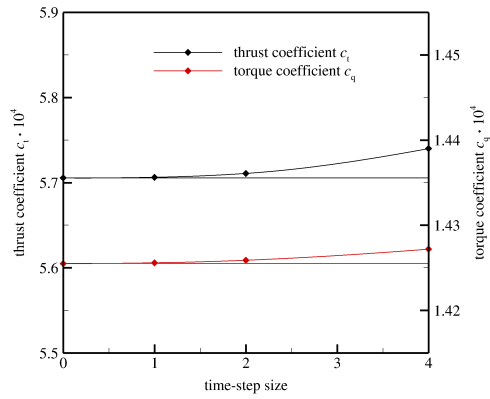
Temporal	[°]/no. of Δt per period	Δt size	c_t $\cdot 10^{-4}$	c_q $\cdot 10^{-4}$	$\Delta_1(c_t/c_q)$ %	$\Delta_0(c_t/c_q)$ %	GCI$_{2-0}$ (c_t/c_q) %	GCI$_{1-0}$ (c_t/c_q) %
Coarse	0.5°/720	4	5.740	1.427	0.6/0.1	0.6/0.1	n.a.	n.a.
Medium	**0.25⁰/1440**	**2**	**5.711**	**1.426**	**0.1/<0.1**	**0.1/<0.1**	**0.1/<0.1**	**n.a.**
Fine	0.125°/2880	1	5.706	1.426	0/0	<0.1/<0.1	n.a.	<0.1/<0.1
Extrapolated	0°/∞	0	5.706	1.426	n.a.	0/0	n.a.	n.a.
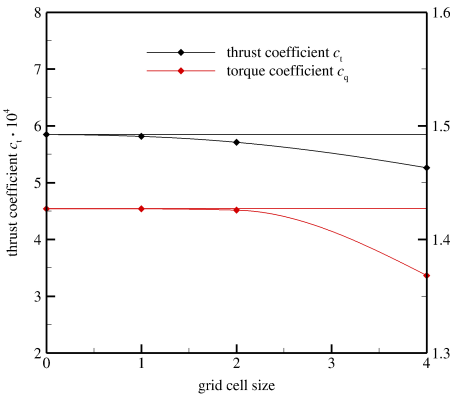
(a) Grid dependency study   (b) Time-step dependency study

FIG. 13. Rotor thrust and torque coefficients ($M_T = 0.794$, $\mathrm{Re}_T = 3.5 \cdot 10^6$, and $\theta = 2°$).

The relative differences % of c_t/c_q between the solutions obtained with the medium (2) and the fine (1) grids (Δ_1) are 1.8% / 0.1%, while comparing against the extrapolated value (Δ_0) are slightly higher (2.3%/0.1%). Confronting the solution of the fine (1) mesh and the extrapolated (0) value gives 0.5%/<0.1%. The corresponding GCI$_{2-0}$ for medium (2) grid is 3.0%/0.1%, while for the fine (1) grid GCI$_{1-0}$ provides 0.7%/<0.1%. Even though the fine (1) mesh is more accurate, it is not economical due to its size, therefore the medium (2) size is chosen for all further investigations. The remaining error bands (3% for c_t and 0.1% for c_q) are expected to have negligible impact on the acoustic predictions presented in the following sections.

The relative differences % of c_t/c_q between the solutions obtained with the medium (2) and the fine (1) time-steps (Δ_1) are 0.1%/<0.1%, while comparing against the extrapolated value (Δ_0) are almost the same, i.e. 0.1%/<0.1%. Confronting the solution of the fine (1) time-step and the extrapolated (0) value gives <0.1%/<0.1%. The corresponding GCI$_{2-0}$ for medium (2) time-step is 0.1%/<0.1%, while for the fine (1) time-step GCI$_{1-0}$ provides <0.1%/<0.1%.

All investigated time-steps are acceptable from the point of view of accuracy, but the medium (2) one is chosen for numerical stability reasons. The remaining error bands (0.1% for c_t and $< 0.1\%$ for c_q) again have negligible impact on the acoustic predictions presented in the following sections.

For the C–T rotor in hover solution with medium grid ($11.39 \cdot 10^6$ volumes) and medium time-step ($0.25°$ of azimuth) the unsteady simulation (restarted from steady oscillating solution) required 140 revolutions until quasi-periodic oscillations were reached (3 days using 4 compute nodes, each node equipped with two 12-core Intel Xeon E5-2670v3 CPUs and 128GB of RAM). To assure that the flow was not experiencing any long-term drift, the simulations were continued and the rotor thrust and torque coefficients averaged in time. For the fine grid of $91.1 \cdot 10^6$ volumes (time-step of $0.25°$) the unsteady simulation (restarted from a steady oscillating solution) required 170 revolutions (20 days using 5 compute nodes). Also here, to make sure that the flow was not experiencing any long-term drift, the simulation was continued and time-averaged. Due to the construction of the numerical grid, designed for fast stabilization of rotor loads, for the initial 1–3 rotor revolutions the unsteady dual-time-stepping scheme required less than 100 sub-iterations (3 orders of magnitude density residual reduction per time-step criterion). For the following revolutions this number was reduced to 1–2 iterations per time-step (even on the fine grid) and the simulations proceeded until the flow state was considered as converged (constant mean values of rotor forces and moments). A single sub-iteration lasted approx. 1 second on the medium and 7 seconds on the fine mesh.

5.4. Comparison of BEMT/CFD results with experimental data

The overall view of the hovering C–T rotor wake is presented in Fig. 14. The iso-surface of the vorticity magnitude $\omega = 80$ $1/s$ and the view are selected in order to visualize the flow phenomena. Even though low-thrust conditions are considered as basic and often used for acoustic investigation of helicopter rotor in-plane harmonic noise (also for all investigated rotors), due to low blade loading a strong blade-vortex interaction (BVI) takes place. Moreover, the close proximity of the following tip vortices is affecting the critical tip flow. Such conditions constitute a major difficulty for efficiency of CFD algorithms and the convergence process becomes very slow.

More than 140 rotor revolutions were required to properly stabilize the thrust and torque coefficients of the investigated rotor. It is worth to mention that even though the tip velocity V_T is subsonic, the relative Mach number of 1.03 is reached locally in the flow-field at the suction side of the blade tip. A zone of $M > 1$ is detected along the last 3% of the blade radius, but the supersonic velocity is so low, that the compression process is almost isentropic and no shock waves are generated.
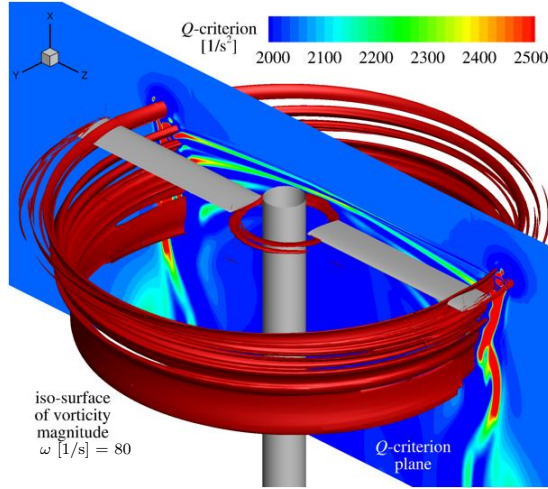
FIG. 14. Rotor wake – vorticity magnitude ω and Q-criterion visualisations ($M_T = 0.794$, $\mathrm{Re}_T = 3.5 \cdot 10^6$, and $\theta = 2^0$).

Figure 15a depicts a comparison of the rotor thrust coefficient c_t vs. the blade collective pitch θ (0°–12°) for both, the test and the BEMT/CFD data. Unfortunately, the experimental c_t is not provided for $\theta = 2°$, therefore an estimated value is used instead. This approximation is based on the assumption of zero thrust at $\theta = 0°$ and on all remaining measured values of c_t for $\theta = 5°, 8°$ and $12°$.
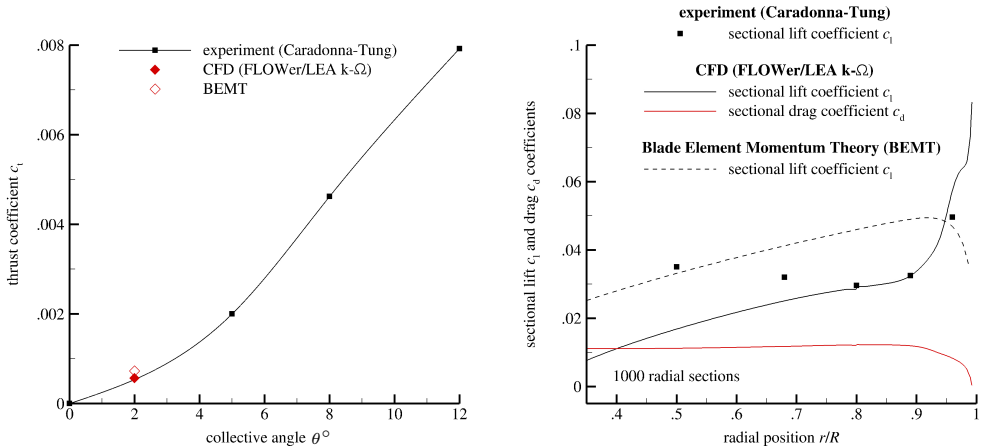

(a) Rotor thrust coefficient c_t
($\theta = 0°$–12°) – total force

(b) Blade sectional lift c_l and drag c_d
coefficients ($\theta = 2°$) – pressure forces

FIG. 15. Rotor aerodynamic loading ($M_T = 0.794$ and $\mathrm{Re}_T = 3.5 \cdot 10^6$).

Table 8. **Rotor thrust and torque coefficients** ($M_T = 0.794$, $\mathrm{Re}_T = 3.5 \cdot 10^6$, **and** $\theta = 2°$**).**

Model rotor data	c_t	c_q
Caradonna–Tung experiment [35]	$5.35 \cdot 10^{-4}$ (estimated)	not available
BEMT [36]	$7.252 \cdot 10^{-4}$	$2.110 \cdot 10^{-4}$
FLOWer/LEA $k - \Omega$ [37]	$5.711 \cdot 10^{-4}$	$1.426 \cdot 10^{-4}$

For $\theta = 2°$ the estimated experimental value of $c_t = 5.35 \cdot 10^{-4}$ is overpredicted using FLOWer/LEA $k - \Omega$ by 7% ($c_t = 5.711 \cdot 10^{-4}$) and by 36% for BEMT ($c_t = 7.252 \cdot 10^{-4}$), see also Table 8. Unfortunately, no experimental torque data is available. It is apparent that the rotor thrust at $\theta = 2°$ is very low and approx. equal to 6.8% of the thrust generated at $\theta = 12°$. For such low collective pitch θ the rotor induced power is negligible, therefore the total rotor power consists mainly of the profile power. Moreover, the thrust and torque coefficients are of similar order of magnitude, which is usually not the case for higher θ settings used for normal operation.

The rotor spanwise loading distribution (due to pressure only) is dominated by the blade-vortex interaction phenomenon (Fig. 15b). The sectional lift c_l and drag c_d coefficients, based on the lift F_l [N] and drag F_d [N] forces exerted on the surface area S, are calculated with the formulas:

$$(5.4) \qquad c_l = \frac{F_l}{\frac{1}{2}\rho V^2 S}, \qquad c_d = \frac{F_d}{\frac{1}{2}\rho V^2 S},$$

where V is the local inflow velocity magnitude. Due to close proximity of the tip, the tip vortices generated by previous blade passages highly influence the effective angle of attack of the blade sections for locations $r/R > 0.75$ (r – radial position). Despite that, the FLOWer/LEA $k - \Omega$ solution satisfactorily fits the experimental values at $r/R = 0.80, 0.89$ and 0.96. On the contrary, more inboard (i.e. at $r/R = 0.50$) the solver prediction exhibits a much larger error compared to the measured value of c_l. Fortunately, not only the hovering rotor total thrust force and shaft torque, but also the acoustic radiation due to loading are dominated by flow development at the outer 25% of the blade span. The computed sectional drag coefficient distribution c_d by FLOWer/LEA $k - \Omega$ is relatively constant along the blade, until the tip, where strong 3D effects dominate. For this particular test case the BEMT cannot predict the local impact of the tip vortices on the blade loading, therefore the estimated sectional lift coefficient is comparable with the experimental data at $r/R = 0.50$ only. Moreover, for $r/R > 0.95$ the decreasing nature of the lift curve is not confirmed by C–T test data (increasing c_l). It suggests that the basic version of BEMT [36] (described in Section 3.1) should be avoided for low-thrust conditions as a rotor

aerodynamic performance analysis tool, because it is not accurate enough. Since it is based on a quasi-2d assumption, it cannot take into account the impact of the blade-tip vortex interaction phenomenon on the tip loading, which is directly used by FW–H code as an acoustic source.

It is worth to mention that the published C–T rotor thrust coefficient and sectional lift coefficient [35] are not obtained with an aerodynamic balance, but are derived using the pressure coefficient c_p distributions recorded at five discrete locations, i.e. at $r/R = 0.5, 0.68, 0.80, 0.89$ and 0.96 (Fig. 16). Low number of experimental pressure taps (located on the pressure and suction sides) at the blade inboard sections (especially at $r/R = 0.5$ and $r/R = 0.68$) may unfavorably affect the accuracy of the c_l calculation. The predicted c_p distributions
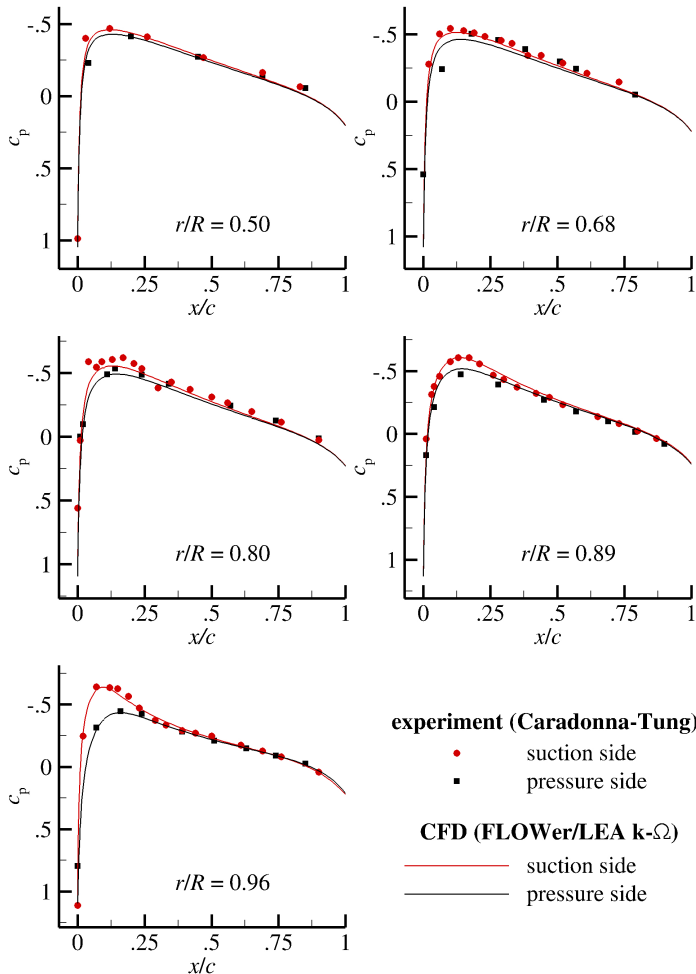

FIG. 16. Rotor blade sectional pressure coefficient ($M_T = 0.794$, $\mathrm{Re}_T = 3.5 \cdot 10^6$, and $\theta = 2°$).

(FLOWer/LEA $k - \Omega$) satisfactorily approximate the experimental points, especially close to the tip (at $r/R = 0.89$ and $r/R = 0.96$), where the comparison is more than acceptable.

The presented detailed validation process of the model C–T helicopter rotor operating in low-thrust hover conditions has proven that the CFD solver (FLOWer/LEA $k - \Omega$) is capable of predicting the aerodynamic loading distribution with sufficient accuracy compared to the available experimental data. Therefore, an analogical computational model is used for acoustic investigation of model rotor of Sargent–Schmitz (S–S) presented in the following sections. On the other hand, it has been verified that the application of BEMT to the C–T rotor case leads to large numerical errors. Still, the BEMT approach is retained in the description, but only because exactly the same basic variant of BEMT had been applied by Sargent and Schmitz for estimation of their model rotor forces and prediction of coupled loading noise generation [30]. As a consequence, apart from the validation of new FW–H code against the experimental (total noise) signal, also a rarely possible code-to-code comparison of separate components of the acoustic pulse (near-field, far-field, thickness, and loading) will be feasible for S–S rotor.

6. Noise prediction for Sargent–Schmitz helicopter rotor

6.1. Source generation methods

The Sargent–Schmitz (S–S) single-bladed model rotor [30] is analyzed with the BEMT method and the ROT version of the CFD solver FLOWer (LEA/$k-\Omega$) using the same methodology as described in the previous section (C–T rotor in low-thrust hover). For BEMT modeling it is assumed that the lift curve slope is equal to $c_{l\alpha} = 2\pi$ and the drag coefficient c_d is constant regardless of the angle of attack α (i.e. $c_d = c_{d0}$), exactly as in [30]. A high value of $c_{d0} = 0.015$ is adopted due to a relatively thick trailing edge of the composite blade. It is not taken into account in the CFD model which is based on a sharp trailing edge simplification.

6.1.1. 1-bladed S–S model rotor geometry. The model rotor consists of 1 untwisted, untapered and rigid blade (and a counter-weight) having rectangular planform and NACA 0012 symmetrical cross-section [30]. The chord length is constant and equal to $c = 0.1016$ m, while the blade radius is $R = 0.9906$ m (aspect ratio of $AR = 9.75$). Various tip Mach numbers M_T ($0.51 \ldots 0.68$) and the blade collective pitch angle of $\theta = 2°$ were investigated. Acoustic pressure signals were recorded at four microphone locations (M1, M2, M3 and M4), but no aerodynamic data is provided though. The computational model of the S–S rotor consists of 2 blades and the artificial hub surface (as in Fig. 9). A decision has been undertaken to take advantage of an existing CFD model (intended for

2-bladed rotors) for prediction of the S–S rotor blade loading. Single-bladed rotor systems are rarely exploited, mainly for the experimental research. The peak amplitude of the acoustic signal at microphone M1 (in-plane), analyzed further in the paper, is primarily dominated by thickness (monopole) component, with a significantly lower secondary contribution from an in-plane loading (dipole). For both rotor designs (1- and 2-bladed) the radiated thickness noise pulse is the same. Moreover, there is practically no difference in radial distribution of the in-plane force (and associated loading noise) between aforementioned configurations. However, due to the increased induced inflow velocity, the 2-bladed rotor exhibits 30% lower blade loading (out-of-plane force) compared to the original design. For the in-plane microphone location (M1) the acoustic consequences of the associated rotor thrust reduction are of tertiary importance only and are quantified (by BEMT) and discussed in more details in Section 6.3.

Keeping the aspect ratio constant ($AR = 9.75$), the geometry is up-scaled to chord length $c = 1$ (radius $R = 9.75$). The radius of the artificial hub is $0.5\,c$, while the inner part of the blade is removed and the blade root is located at $1.0\,c$. No information is provided regarding the tip or the root cut-off shapes, so flat surfaces are applied there. The blade trailing edge is sharp (zero thickness) and the pitch axis is set to $0.25\,c$.

6.1.2. Numerical model description The computational domain (160 blocks) and block-structured C–H–H grid ($11.39 \cdot 10^6$ of control volumes) are analogous to the C–T rotor computational model (see Figs. 10 and 11). Due to the increased rotor aspect ratio ($AR = 9.75$), in total 89% of cells exhibit the most desired orthogonality level ($75°$–$90°$), with additional 7% in the range $60°$–$75°$. Due to the adopted topology, the remaining 4% of lower quality cells cannot be improved. The maximum aspect ratio is 6080. The same type of boundary conditions, as well as the computational domain size in each direction ($3\,R$), are applied as for the C–T rotor analysis (Fig. 12). The S–S rotor dimensions and operating conditions are summarized in Table 9.

A low-thrust case is investigated with the collective pitch setting $\theta = 2°$ and rotational speed of $2169\,RPM$ ($M_T = 0.661$, $\mathrm{Re}_T = 1.6 \cdot 10^6$). The unavailable ambient conditions are fixed at Standard Day Conditions (SDC), i.e. $T_0 = 288.15$ K and $P_0 = 101325$ Pa. Also here, the re-scaling procedure of the blade chord to $c = 1$ necessitates a modification to the rotor operating conditions (see Table 9). Again, the FLOWer default values of the inlet eddy viscosity ratio of 0.001 and of the turbulence level of 0.5% are adopted. The grid resolution and the time-step size dependency studies have been conducted, but are not presented here. The medium grid ($11.39 \cdot 10^6$ volumes) and the time-step Δt of the numerical scheme corresponding to $0.25°$ of rotation (i.e. $\Delta t = 1.89 \cdot 10^{-4}$ s, 1440 time-steps per revolution) were selected for further studies. Again, due to

Table 9. S–S model rotor dimensions and operating conditions.

Parameter	Experimental model	CFD model
Rotor radius, R [m]	0.9906	9.75
Blade chord length, c [m]	0.1016	1.0
Rotor aspect ratio, AR	9.75	9.75
Blade collective angle, θ [°]	2.0	2.0
Ambient pressure, P_0 [Pa]	101325	10530
Ambient temperature, T_0 [K]	288.15	288.15
Ambient density, ρ_0 [kg/m^3]	1.22	0.127
Ambient viscosity, μ_0 [Pa · s]	$1.79 \cdot 10^{-5}$	$1.79 \cdot 10^{-5}$
Ambient speed of sound, c_0 [m/s]	340.3	340.3
Rotational speed, RPM	2169	220.3
Tip Mach number, M_T	0.661	0.661
Tip Reynolds number, Re_T	$1.6 \cdot 10^6$	$1.6 \cdot 10^6$
Tip velocity, V_T [m/s]	225.0	225.0
Frequency of rotation, f_{rot} [Hz]	36.14	3.672
Period of rotation, T [ms]	27.7	272

Table 10. Rotor thrust c_t and torque c_q coefficients ($M_T = 0.661$, $\mathrm{Re}_T = 1.6 \cdot 10^6$, and $\theta = 2°$).

Model rotor data	c_t	c_q	c_t per blade	c_q per blade
FLOWer/LEA $k - \Omega$ [37] (2 blades)	$5.071 \cdot 10^{-4}$	$0.925 \cdot 10^{-4}$	$2.535 \cdot 10^{-4}$	$0.462 \cdot 10^{-4}$
BEMT [36] (2 blades)	$6.074 \cdot 10^{-4}$	$1.320 \cdot 10^{-4}$	$3.037 \cdot 10^{-4}$	$0.660 \cdot 10^{-4}$
BEMT [36] (1 blades)	$4.267 \cdot 10^{-4}$	$0.672 \cdot 10^{-4}$	$4.267 \cdot 10^{-4}$	$0.672 \cdot 10^{-4}$

the low thrust coefficient value, more than 140 rotor revolutions were required to properly stabilize the thrust c_t and torque c_q coefficients.

Table 10 depicts a comparison of the c_t and c_q predicted by CFD (FLOWer/ LEA $k - \Omega$) and by BEMT. Again, the BEMT method overpredicts the rotor thrust by 20% compared to the validated CFD methodology (for the C–T model rotor this discrepancy is equal to 27%). Due to the high value of $c_{d0} = 0.015$, assumed for the composite blade constructed with a thick trailing edge [30], the torque coefficient c_q computed by BEMT is also 43% higher than derived with the FLOWer solver (sharp trailing edge blade). The data confirms that the basic variant of the BEMT method ($c_{l\alpha} = 2\pi$ and $c_d = c_{d0} = 0.015$ [36]), applied in the acoustic research of SARGENT and SCHMITZ [30], delivers only a crude approximation of the forces acting on the rotor blades. As it has already been explained the thrust coefficient c_t value per blade for the 2-bladed rotor is 29% lower than for the 1-bladed one operating in exactly the same conditions

(BEMT). This difference for the torque coefficient c_q is less than 2% though (negligible). It is necessary to mention that the ambient conditions for BEMT are modified compared to the presented CFD model (Table 9), which is described in more detail in Section 6.2. Also the blade surface pressure distribution (CFD) is re-scaled to updated T_0 and P_0. The resultant BEMT and CFD loadings (Table 10) are given as input to the FW–H code to predict loading noise.

6.2. Thickness and loading noise prediction

A detailed comparison of the FW–H acoustic code (Section 3.4) predictions (component-wise) with the reference code (University of Maryland) [30] solutions is presented for S–S rotor in Fig. 17. Since the LF-IPH noise is of primary interest, the signal of microphone M1 (located at $2.40\,R$ from the rotation axis and $1.63\,c$ above the rotor plane) is chosen for analysis. For thickness noise calculation, the blade surface grid is extracted directly from the 3D CFD model, with its each cell constituting a separate acoustic source panel. For the monopole radiation, spatial and temporal discretization dependency studies are conducted using coarse (2016), medium (6864), and fine (25200) grids, as well as coarse $(T/360)$, medium $(T/720)$, and fine $(T/1440)$ time-steps. The fine grid (25200) and fine time-step $(T/1440)$ are selected for all subsequent thickness noise predictions due to improved amplitude and phase of the resultant signal. This computation lasted for 34 hours using a high-end desktop computer (AMD Ryzen Threadripper 3960X, 24 core CPU and 256GB of RAM). However, because of the unknown experimental ambient conditions, the temperature is calibrated first and fixed at $T_0 = 286\,K$ to match the phase of the main pressure pulse (dependence of speed of sound on temperature). Next, the pressure is set to $P_0 = 106500\,Pa$ to improve
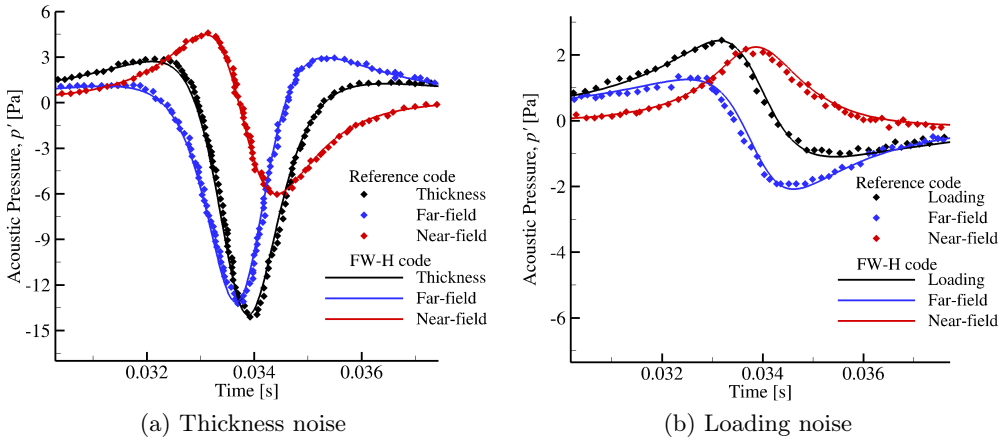

(a) Thickness noise   (b) Loading noise

FIG. 17. Comparison of FW–H code acoustic signal components prediction with reference code [30].

the peak amplitude. The alteration of T_0 and P_0 only slightly affects the phase and peak amplitudes, the basic shape of the pulse is retained [43]. Additionaly, it does not change the rotor tip Mach number, therefore has rather low impact on the rotor performance (loading) through the tip Reynolds number (also not provided). The total signal is depicted in Fig. 17a (thickness) along with its near- and far-field components, for both the FW–H and the reference code.

In order to compare directly loading noise predictions (FW–H and reference codes), exactly the same BEMT method is implemented (Section 3.1) and identical input parameters and blade/time disretizations (95 radial sections and time-step of $T/360$) are applied as described in [30]. Moreover, the resultant spanwise distribution of the aerodynamic forces is transferred to the FW–H code using the compact chord assumption. For the loading noise emission, the ambient conditions are compatible with the thickness noise analysis (i.e. $T_0 = 286\,\text{K}$ and $P_0 = 106500\,\text{Pa}$). The total signal is depicted in Fig. 17b (loading) along with its near- and far-field components, for both the FW–H and the reference code.

The thickness noise is generated due to the chordwise distribution of elementary sources and sinks which emit perturbations of opposite signs that arrive at the observer at different times (as described in Section 4.1). As a result of phase mismatch, a characteristic symmetrical large negative pressure pulse (surrounded by two smaller positive humps) is radiated [6]. The rotating blade spanwise distribution of the aerodynamic forces (mainly in-plane and out-of-plane components) generate loading noise (as described in Section 4.2). Due to the observer location in the acoustic near-field of the rotor, both components (i.e. near- and far-field) are significant for both thickness and loading noise estimations. However, it is the far-field one which is predominant in terms of the total acoustic signal waveform. Even though the near-field component has a noticeable impact on the final pulse amplitude and phase, the nature of the far-field one is preserved. On the other hand, the contribution of loading noise to the total acoustic signal is small compared to the thickness noise for microphone M1 location (almost in-plane). Taking into consideration the approximations and simplifications involved (e.g. differences in blade surface discretization, calibration procedure for ambient conditions, and two separate in-house numerical codes involved), the FW–H acoustic code predictions are in satisfactory agreement both qualitatively and quantitatively with the reference code solutions (near-/far-field/total and thickness/loading components).

6.3. Loading noise prediction

Further validation of the S–S rotor loading noise prediction by the FW–H code is conducted against the analytical solutions. The analytical acoustic signals are derived based on a linear combination of known elementary solutions

(Eq. (2.3) and Section 4.2) for point sources of momentum (forces) distributed along the rotating blade radius and positioned at the quarter-chord (compact chord assumption). Aerodynamic forces are computed with the BEMT method (95 radial sections) and transferred directly to the FW–H and the analytical loading codes for acoustic post-processing. Because the BEMT outputs in-plane and out-of-plane components of the forces separately, their impact on the total loading noise emission may be assessed (see Fig. 18). Moreover, the FW–H solutions (near-field and far-field) are not only compared with the analytical solutions, but also with the reference waveform [30]. For the near in-plane microphone M1 location both in-plane (torque generation) and out-of-plane (thrust generation) forces contribute to the total loading noise signature. The radial (spanwise) forces are not considered here.
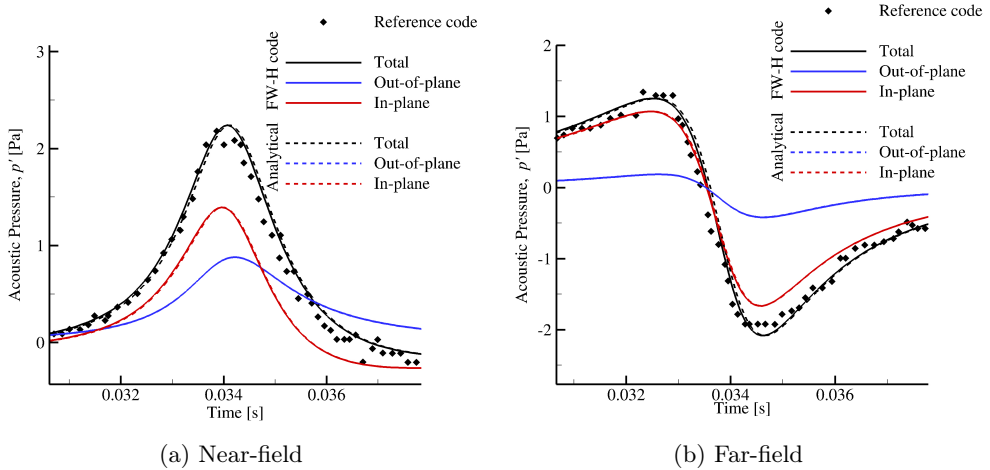

(a) Near-field   (b) Far-field

Fig. 18. The FW–H and analytical code loading noise predictions against reference [30].

For the near-field component (Fig. 18a), both the in-plane and out-of-plane forces comparably contribute to the total acoustic signal. However, the in-plane force contribution is predominant over the out-of-plane force contribution (3 times higher amplitude) for the far-field component (Fig. 18b). Since the shape and phase of the acoustic pulses generated by both types of forces are similar, their linear summation leads to a constructive effect (increase of amplitude) for near- and far-field noise components. It is important to note that the out-of-plane (thrust) force contribution to the loading noise for microphone M1 is significant only because of the near-field observer location and may not be noticeable in the acoustic far-field. It is evident that the FW–H code predictions are equivalent to the presented analytical solutions for both near and far-field components of the loading noise signal. As a direct consequence, also the resultant acoustic pressure pulses (summation of in-plane and out-of-plane

forces contribution) are in good agreement with the reference code data. It can be noted that for BEMT + FW–H (compact chord), the speed-up of loading noise prediction is 7 compared to the full CFD + FW–H analysis. Moreover, for the analytical code (also based on BEMT) this speed-up is even higher (i.e. 32).

For the final estimation of the loading distribution (used in Section 6.4 for experimental validation) of the single-bladed S–S rotor, a 2-bladed CFD model is adopted (as described in Section 6.1). The acoustic consequences of this choice are quantified not only in terms of the near- and far-field components of the signal but also divided into the in-plane and out-of-plane force contributions. For comparison purposes the reference data is presented as well. BEMT blade loading solutions obtained for a 1- and 2-bladed rotors are used as input to the analytical loading noise prediction code. The resultant acoustic pressure signal components are presented in Fig. 19. As has already been presented in Fig. 18, the analytical code provides equivalent results to the FW–H analysis at a fraction of the computational cost.
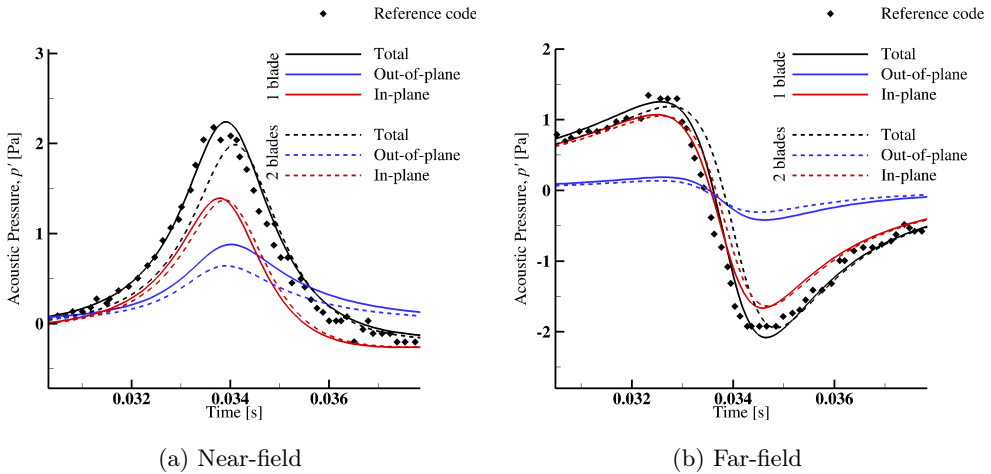

(a) Near-field   (b) Far-field

FIG. 19. Analytical code predictions of loading noise components for 1- and 2-bladed rotors.

For the near-field and far-field components of the loading noise, the main pressure pulses recorded at microphone M1 location and emitted by the 1- and 2-bladed rotors are similar in shape. Still, the 11% (near-field) and 6% (far-field) differences in peak amplitude are present that are accompanied by a slight phase shift between both solutions (and the reference data). This deviation is attributed mainly to the variability in the acoustic emission due to the out-of-plane force. The 2-bladed rotor generates higher thrust compared to the 1-bladed design when operating conditions are fixed. It results in increased downwash (induced velocity) and therefore leads to the reduction of the effective angle of attack of

each blade section. Hence, the reduced loading (per blade) and lower associated loading noise levels are observed. Since the c_d is almost constant for near-zero inflow angles, the blade sectional in-plane force distribution is practically not affected by the choice of the model (1- or 2-bladed) and the related acoustic emission of both configurations is almost identical. The LF-IPH noise pulse consists primarily of the thickness noise with a secondary contribution of the steady loading noise (Fig. 17). The rotor loading noise due to the in-plane force (torque generating) is not affected by the computational model choice (1- or 2-bladed). However, the quantified difference in out-of-plane (thrust generating) force distributions has only a tertiary importance in terms of the in-plane acoustic emission and may be safely neglected.

6.4. Total noise prediction

The total acoustic pressure signals obtained from linear summation of p_T and p_L at the correct observer time are compared against the reference solution (black diamonds) and the experimental data (red triangles) in Fig. 20a. The total signal is characterized by a large negative pressure pulse surrounded by two smaller positive humps (asymmetric), similar to the dominating thickness component shape (for subsonic tip speeds and near in-plane observer locations). The loading noise predictions of FW–H code based on both source generation methods BEMT (blue line) and CFD (green line) are added together with thickness noise to obtain total signals (marked as BEMT + FW–H and CFD + FW–H). The loading noise not only slightly alters the positive humps (located before and after the main event), but also decreases the peak amplitude of the negative pulse.
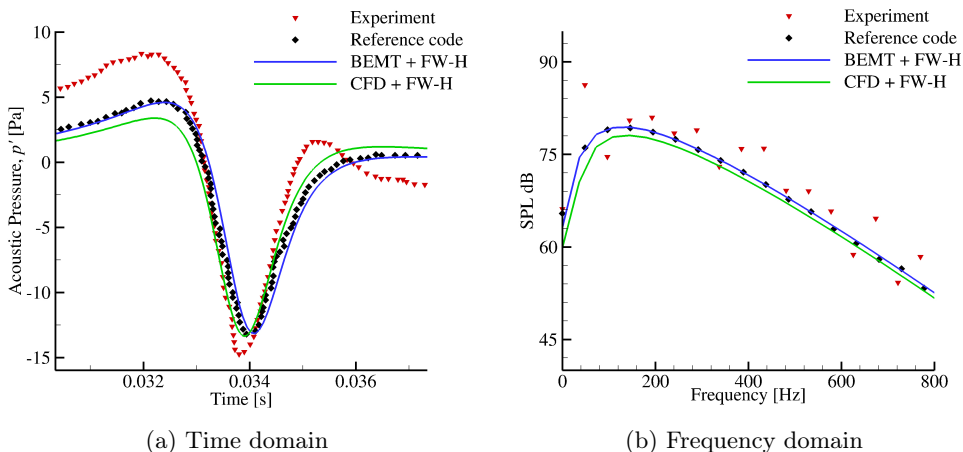

(a) Time domain   (b) Frequency domain

Fig. 20. Total acoustic signal analysis for Sargent–Schmitz rotor.

In the time domain, the width and amplitude of the BEMT + FW–H total acoustic signal is matching the reference code prediction well. However, there is a small phase shift between both solutions (approx. equal to 0.2 ms), possibly due to tiny misalignments of loading and thickness (near- and far-field) components and the reference data (noticeable in Fig. 17). It is important to keep in mind that exactly the same methodology (BEMT, 95 radial sections) is used for both loading noise predictions (reference and BEMT + FW–H), but the presented thickness noise analysis is based on the CFD grid of much higher resolution compared to the surface discretization used in [30]. The calculated total acoustic signals based on BEMT (BEMT + FW–H) and CFD (CFD + FW–H) blade loadings are similar in terms of the negative peak-amplitude. However, apart from a different phase (by approx. 0.3 ms), the leading, rising edge positive peak is reduced (by approx. 1 Pa) between BEMT + FW–H and CFD + FW–H solutions. At the same time, the right hand side positive peak is increased by a similar value (approx. 1 Pa). The origin of this difference is a primarily significant overprediction of the blade loading by basic BEMT method (as has been presented in Section 5.4). Moreover, the two-bladed CFD model exhibits lower out-of-plane component of the aerodynamic force (and of the associated loading noise) compared to the single-bladed design (see Section 6.3). In terms of the main negative LF-IPH pulse, the CFD + FW–H approach somewhat improves the peak amplitude and phase compared to the experimental data, while becoming slightly less consistent with the reference and BEMT + FW–H signals.

It is worth to emphasize that in contrast to the theoretical data of Fig. 20 (reference and in-house FW–H code predictions), the experimental data is subjected to significant low-frequency acoustic reflections that affect the investigated noise signature. University of Maryland Acoustic Chamber (UMAC) is a small facility devoted to helicopter rotor acoustic investigations [30]. The testing space is covered by acoustic wedges with strategic placement of additional absorbing material at key reflection surfaces. Moreover, the choice of a single-bladed rotor and microphones placement are key features allowing for separation of the main pulse from the reflected signatures thus enabling quantitative LF-IPH noise measurements. Even though the waveform shape is highly affected before and after the negative peak, the time history reflections are separated from the main pulse of interest. Still, the peak amplitude of the negative pulse is slightly underpredicted by both BEMT + FW–H (10%) and CFD + FW–H (9%) analysis compared to the experimental points and in-line with the reference code result (9%).

The SPL spectra are presented in Fig. 20b for the lowest 20 rotor harmonics (up to 800 Hz). All signals are dominated by low frequencies, with maxima present at approx. 150 Hz. Due to presence of acoustic reflections not only the experimental SPL curve (red triangles) reveals wavy character and is shifted upwards, but it also exhibits a dominating low-frequency component (2nd har-

monic) not present in the theoretical solutions. Still, the BEMT + FW–H (blue line) and CFD + FW–H (green line) modelling results satisfactorily match the reference spectrum (black diamonds).

The overall sound pressure levels calculated for all depicted cases are summarized in Table 11. The presented values (OASPL from p_{rms}) for the reference code and the experiment are derived based on time domain signals extracted from figures presented in [30] and may constitute only an approximation of the measured data. Due to presence of significant wall reflections in UMAC, the experimental OASPL (106.4 dB) is underpredicted by 2.6 dB–4.4 dB for the reference (103.8 dB), BEMT + FW–H (103.6 dB), and CFD + FW–H (102 dB) signals. However, the difference in OASPL between both theoretical approaches and the reference code is equal to 0.2 dB (BEMT + FW–H) and 1.8 dB (CFD + FW–H). The integration of the SPL spectra of Fig. 20b results in OASPL values (OASPL from SPL) differing by less than 0.5 dB compared to the time-domain analysis (OASPL from p_{rms}).

Table 11. Overall sound pressure level (OASPL) for Sargent–Schmitz rotor.

Model rotor data	OASPL from p_{rms} dB	OASPL from SPL dB
Experiment [30]	106.4	106.7
Reference code [30]	103.8	103.3
BEMT + FW–H	103.6	103.4
CFD + FW–H	102.0	102.0

7. Summary and conclusions

An in-house, post-processing, aeroacoustic code based on the FW–H acoustic analogy is developed. The integral solution in time domain known as Farassat Formulation 1A is implemented to predict thickness and loading noise for rotating bodies in a subsonic motion (e.g. helicopter rotor blades in hover). The code is validated for elementary sources against known analytical solutions. A rotating source-sink pair (distributed) that models the mechanism of thickness noise generation is validated against the analytical solutions derived for moving point sources of mass. A rotating out-of-plane (thrust) and in-plane (torque) distributed forces that model the mechanism of loading noise generation are validated against the analytical solutions derived for moving point forces (sources of momentum). Acoustic pressure signals predicted by FW–H code (in time and frequency domains) are in satisfactory agreement with accuracy of 0.5% in terms of the peak amplitude of p', p_{rms} and frequency and 0.2 dB for OASPL. Due to the partial acoustic cancellation involved, the obtained acoustic solutions prove to be time-consuming and sensitive to the input parameters, the source dimensions, the density of the surface grid, and the time-step size of the FW–H analysis.

The developed acoustic code is used to predict numerically Low-Frequency In-Plane Harmonic (LF-IPH) noise of a model helicopter rotor of Sargent and Schmitz in low-thrust hover conditions that is compared with available experimental data and reference code solutions from University of Maryland. Two methods of blade surface loading estimation are introduced – BEMT and CFD and validated for a 2-bladed rotor of Caradonna and Tung operating in similar conditions. Due to the inability of the basic BEMT method to capture the blade-vortex interaction phenomenon, the blade loading is overpredicted compared to the experimental data. On the other hand, the CFD methodology adopting RANS equations (here using FLOWer solver with LEA $k - \Omega$ turbulence closure) is capable of predicting the rotor induced inflow velocity and far-field flow structure, thus allowing for more accurate estimation of blade sectional loads compared to the basic BEMT method.

For calculation of the thickness noise of the Sargent–Schmitz rotor, the CFD surface mesh is used directly in all cases. For in-plane loading noise analysis, the BEMT and CFD blade loadings are given as input for the FW–H code. The BEMT + FW–H solution (compact chord assumption) proves to be equivalent to the reference code estimation in terms of near- and far-field terms. Moreover, the contribution of the in-plane (torque) and out-of-plane (thrust) forces to loading noise (near- and far-field terms) is quantified. For almost in-plane microphone location the signals peak amplitude is dominated by the thickness component, with secondary contributions from the in-plane and out-of-plane forces. The CFD analysis is conducted using available 2-bladed computational model (experimental rotor is 1-bladed). The difference in induced inflow velocity for both configurations affects slightly the lower, out-of-plane (thrust) component of the blade sectional force only and is noticeable mainly in the near-field term (reduced significance while moving towards the acoustic far-field). Therefore, for a near-zero blade pitch setting (low-thrust), the acoustic consequences of this assumption are of tertiary importance. Finally, the BEMT + FW–H loading noise prediction is compared with analytical solutions (rotating spanwise distribution of point sources of momentum).

The computed (BEMT + FW–H) total noise signature (thickness and loading) is in satisfactory agreement with the reference code data both qualitatively and quantitatively (near- and far-field terms). However, lower blade loading predicted by CFD impacts the comparison with the reference signal (based on BEMT), therefore the CFD + FW–H acoustic solution is also affected. Analyzed total acoustic signals compare well in terms of the main pulse width and shape with the experimental data. The underprediction in the peak negative amplitude and in the OASPL is attributed to low-frequency reflections present in the acoustic chamber that are not modeled by FW–H analogy.

The relative ease of direct application of the code to existing CFD models and results and the flexibility in its use, allow it to be utilized for various rotating (open space) configurations (such as propeller, helicopter, and wind turbine rotors) and to investigate the acoustic penalty of various flow control strategies and methods.

Appendix

Grid and time-step resolution dependencies along with the execution time for a rotating source (Section 4.1) and rotating in-plane forces (Section 4.2) are presented in the Tables A1 and A2. The characteristics of sound such as the p_{rms}, OASPL and the frequency of the first harmonic are presented below. The error percentages are computed against the analytical solution.

Table A1. Convergence studies (grid and time-step) for a rotating source.

Monopole	Resolution	p_{rms}	OASPL	Frequency	Run-time
Analytical	Very fine	0.313 Pa	83.879 dB	36.082 Hz	16 s

Code	Resolution	p_{rms} Error %	OASPL error dB	Frequency error %	Run time [min]
FW–H grid dependency (fine time-step)	Coarse	3.3	0.3	0.5	11
	Medium	0.9	0.1	0.5	14
	Fine∗	0.3	<0.1	0.4	44
FW–H time-step dependency (fine grid)	Coarse	0.6	0.1	0.6	4
	Medium	0.5	<0.1	0.5	17
	Fine∗	0.3	<0.1	0.4	44

∗ indicates an identical case.

Table A2. Convergence studies (grid and time-step) for a rotating in-plane force.

Dipole	Resolution	p_{rms}	OASPL	Frequency	Run-time
Analytical	Very fine	1.414 Pa	96.99 dB	36.367 Hz	33 s

Code	Resolution	p_{rms} Error %	OASPL error dB	Frequency error %	Run time [min]
FW–H grid dependency (fine time-step)	Coarse	1.04	0.1	<0.1	3
	Medium	0.66	<0.1	<0.1	9
	Fine∗	0.15	<0.1	<0.1	34
FW–H time-step dependency (fine grid)	Coarse	0.29	<0.1	0.7	3
	Medium	0.17	<0.1	0.1	11
	Fine∗	0.15	<0.1	<0.1	34

∗ indicates an identical case.

From the data analysis of the tables, we can infer that for all elementary cases, an insufficient spatial resolution affects the peak amplitude of the signal thus impacting p_{rms} and OASPL values. The time-step resolution predominantly affects the frequency and the phase of the signal. The error in phase difference is not an issue in case of individual sources but becomes very significant when distributed source addition is required. For instance, a tiny phase shift error in individual source/sink leads to non trivial errors while adding source-sink pair that mimics thickness noise generation. Hence, even though fine time-step (T/720) satisfies the criterion of error <0.5%, to better fit the SPL curves and phase of the added signal, very fine time-step (T/5760) solutions are presented in Sections 4.1 and 4.2.

The dependencies (grid and time-step) are presented for the rotating source case only as the source and sink grids (sphere) are identical (Fig. 2). The total signal emitted by the source-sink pair is obtained by adding the converged solution from individual source and sink (Fig. 5). The phase of the signal is the most important characteristic for addition thus necessitating very fine time-steps (T/5760). It can also be noted that the computation time is a function mainly of the time-step thus increasing the resolution in time increases the run time.

Similarly, only the second case (rotating in-plane force) dependencies are presented here since the grid used for both the in-plane and out-of-plane forces are identical (Fig. 6). Similar trends in the characteristics are observed for both cases. Also here, the fine time-step solution (∗) satisfies the <0.5% error criterion (see Tables 3 and 4), but, to improve the phase of the signal and to be compatible with the previous case (Section 4.1), solutions of very fine time-step (T/5760) are presented in Figs. 7 and 8. The acoustic computation time for the converged in-plane force (34 min) is lesser than the run time for the converged rotating source prediction (44 min). This is because the rotating source of mass grid has more surface panels (1536 cells) than the rotating in-plane force grid (1280 cells), previously described in Section 4.

Acknowledgments

References

1. M.V. Lowson, *Progress towards quieter civil helicopters*, The Aeronautical Journal, **96**, 956, 209–223, 1992.

2. B.W. Sim, R.D. Janakiram, N.L. Barbely, E. Solis, *Reduced in-plane, low-frequency noise of an active flap rotor*, Journal of the American Helicopter Society, **59**, 2, 022002, 1–17, 2014.

3. Y. Shi, T. Li, X. He, L. Dong, G. Xu, *Helicopter rotor thickness noise control using unsteady force excitation*, Applied Sciences, **9**, **1351**, 03, 2019.

4. P. Beaumier, B. Van Der Wall, K. Pengel, C. Kessler, M. Gervais, Y. Delrieux, J.F. Hirsch, P. Crozier, *From ERATO basic research to the blue edge*$^{\text{tm}}$ *rotor blade: an example of virtual engineering*, Rotorcraft Virtual Engineering Conference, hal-01413109, 2016.

5. H.H. Hubbard, *Aeroacoustics of Flight Vehicles: Theory and Practice, Vol. 1: Noise Sources*, NASA Langley Reference Publication, 1258, 1991.

6. F. H. Schmitz, *The challenges and possibilities of a truly quiet helicopter, 29th Alexander A. Nikolsky honorary lecture*, Journal of the American Helicopter Society, **61**, 4, 1–33, 2016.

7. F.H. Schmitz, Y.H. Yu, *Helicopter impulsive noise, theoretical and experimental status*, Journal of Sound and Vibration, **109**, 3, 361–422, 1986.

8. D.A. Boxwell, F.H. Schmitz, *Full-scale measurements of blade-vortex interaction noise*, Journal of the American Helicopter Society, **27**, 11–27, 1982.

9. T.F. Brooks, M.A. Marcolini, P.S. Dennis, *Main rotor broadband noise study in the DNW*, Journal of the American Helicopter Society, **34**, 2, 3–12, 1989.

10. K.S. Brentner, F. Farassat, *Modeling aerodynamically generated sound of helicopter rotors*, Progress in Aerospace Sciences, **39**, 2, 83–120, 2003.

11. B.R. Jones, W.A. Crossley, A.S. Lyrintzis, *Aerodynamic and aeroacoustic optimization of rotorcraft airfoils via a parallel genetic algorithm*, Journal of Aircraft, **37**, 11, 1088–1096, 2000.

12. G. Wilke, *Quieter and greener rotorcraft: concurrent aerodynamic and acoustic optimization*, CEAS Aeronautical Journal, **12**, 495–508, 2021.

13. S. Moreau, *The third golden age of aeroacoustics*, Physics of Fluids, **34**, 3, 031301, 2022.

14. C.K.W. Tam, *Computational aeroacoustics: an overview of computational challenges and applications*, International Journal of Computational Fluid Dynamics, **18**, 6, 547–567, 2004.

15. A.S. Lyrintzis, *Surface integral methods in computational aeroacoustics – from the (CFD) near-field to the (acoustic) far-field*, International Journal of Aeroacoustics, **2**, 2, 95–128, 2003.

16. J.W. Kim, D.J. Lee, *Generalized characteristic boundary conditions for computational aeroacoustics*, AIAA Journal, **38**, 11, 2040–2049, 2000.

17. T. Colonius, S.K. Lele, *Computational aeroacoustics: progress on nonlinear problems of sound generation*, Progress in Aerospace Sciences, **40**, 6, 345–416, 2004.

18. S.K. Lele, *Computational aeroacoustics – A review*, American Institute of Aeronautics and Astronautics, 35th Aerospace Sciences Meeting and Exhibit, 1997.

19. C. Hansen, *Fundamentals of acoustics*, American Journal of Physics, **19**, 1951.

20. M. J. Lighthill, *On sound generated aerodynamically I. General theory*, Proceedings of the Royal Society of London A: Mathematical, Physical and Engineering Sciences, **211**, 1107, 564–587, 1952.

21. N. Curle, *The influence of solid boundaries upon aerodynamic sound*, Proceedings of the Royal Society of London A: Mathematical, Physical and Engineering Sciences, **231**, 1187, 505–514, 1955.

22. J.E. Ffowcs Williams, D.L. Hawkings, *Sound generation by turbulence and surfaces in arbitrary motion*, Philosophical transactions of the Royal Society of London A: Mathematical, Physical and Engineering Sciences, **264**, 321–342, 1969.

23. F. Farassat, K.S. Brentner, *The uses and abuses of the acoustic analogy in helicopter rotor noise prediction*, Journal of the American Helicopter Society, **33**, 1, 29, 1988.

24. Z. Huang, L. Siozos-Rousoulis, T. De Troyer, G. Ghorbaniasl, *Helicopter rotor noise prediction using a convected FW-H equation in the frequency domain*, Applied Acoustics, **140**, 11, 122–131, 2018.

25. O. Szulc, *Rotorcraft Thickness Noise Control*, Archives of Mechanics, **73**, 4, 391–417, 2021.

26. D.A. Smith, A. Filippone, G.N. Barakos, *Acoustic analysis of counter-rotating open rotors with a locked blade row*, AIAA Journal, **58**, 10, 4401–4414, 2020.

27. E. Fabiano, A. Mishra, D.J. Mavriplis, K. Mani, *Time-dependent aero-acoustic adjoint-based shape optimization of helicopter rotors in forward flight*, 57th AIAA/ASCE/AHS/ASC Structures, Structural Dynamics, and Materials Conference, 2016.

28. F. Farassat, *Derivation of formulations 1 and 1A of Farassat*, NASA Technical Report, 214853 (TM-2007-214853), 1–25, 2007.

29. S.W. Rienstra, A. Hirschberg, *An Introduction to Acoustics*, Technische Universiteit Eindhoven, **0103**, 2001.

30. D. Sargent, F.H. Schmitz, *Fundamental experimental studies supporting active-jet acoustic control of in-plane rotor harmonic noise*, Journal of Aircraft, **51**, 2, 434–446, 2014.

31. G. Gopalan, F.H. Schmitz, *Understanding far field near-in-plane high speed harmonic helicopter rotor noise in hover and forward flight: governing parameters and design trends*, American Helicopter Society Technical Specialists' Conference, 2008.

32. F. Farassat, *Introduction to generalized functions with applications in aerodynamics and aeroacoustics*, NASA Technical Paper, **3248**, 1994.

33. F. Farassat, *The Kirchhoff Formulas for moving surfaces in aeroacoustics – the subsonic and supersonic cases*, NASA Technical Memorandum, **110285**, 1996.

34. F. Farassat, *Theory of noise generation from moving bodies with an application to helicopter rotors*, NASA Technical Report, **R-451**, 1975.

35. F. Caradonna, C. Tung, *Experimental and analytical studies of a model helicopter rotor in hover*, Technical Memorandum, NASA Ames, **81232**, 1981.

36. J.G. Leishman, *Principles of Helicopter Aerodynamics, Chapter 3: Blade Element Analysis*, Cambridge University Press, 115–170, Cambridge, 2006.

37. J. Raddatz, J.K. Fassbender, *Block structured Navier–Stokes solver FLOWer*, [in:] *MEGAFLOW – numerical flow simulation for aircraft design*, Notes on Numerical Fluid Mechanics and Multidisciplinary Design, **89**, 27–44, 2005.

38. T. Rung, H. Lübcke, M. Franke, F. Xue, F. Thiele, S. Fu, *Assessment of Explicit Algebraic Stress Models in Transonic Flows*, International Symposium on Engineering Turbulence Modelling and Measurements, 1999.

39. T. Suresh, O. Szulc, P. Flaszynski, P. Doerffer, *Prediction of helicopter rotor noise in hover using FW-H analogy*, Journal of Physics: Conference Series, **1101**, 2018.

40. N.A.R.N. Mohd, G.N. Barakos, *Computational aerodynamics of hovering helicopter rotors*, Jurnal Mekanikal, **34**, 16–46, 2012.

41. F. Tejero, P. Doerffer, P. Flaszynski, O. Szulc, *Passive flow control application for rotorcraft in transonic conditions*, International Journal of Numerical Methods for Heat and Fluid Flow, **5**, 28, 1080–1095, 2018.

42. P.J. Roache, *Verification and Validation in Computational Science and Engineering*, Hermosa Publishers, 107–142, Sorocco, New Mexico, 1998.

43. E. Greenwood, F.H. Schmitz, *The effects of ambient conditions on helicopter rotor source noise modeling*, American Helicopter Society 67th Annual Forum, **05**, 2011.